(1)

PPPL-1660

PPPL--1660

DE82 013994

SOFT X-RAY MEASUREMENTS FROM THE PDX TOKAMAK

By

E.H. Silver, M. Bitter, K. Brau, D. Eames, A. Greenberger, K.W. Hill, D.M. Meade, W. Roney, N.R. Sauthoff and S. von Goeler

MAY 1982

PLASMA PHYSICS LABORATORY

PRINCETON UNIVERSITY

PRINCETON, NEW JERSEY

PREPARED FOR THE U.S. DEPARTMENT OF ENERGY, UNDER CONTRACT DE-AC02-76-CHO-3073.

NOTICE

Printed in the United States of America.

Available from:

National Technical Information Service
U. S. Department of Commerce
5285 Port Royal Road
Springfield, Virginia 22151

Price: Printed Copy $ * ; Microfische $3.50

*PAGES	NTIS Selling Price
1-25	$5.00
26-50	$6.50
51-75	$8.00
76-100	$9.50
101-125	$11.00
126-150	$12.50
151-175	$14.00
176-200	$15.50
201-225	$17.00
226-250	$18.50
251-275	$20.00
276-300	$21.50
301-325	$23.00
326-350	$24.50
351-375	$26.00
376-400	$27.50
401-425	$29.00
426-450	$30.50
451-475	$32.00
476-500	$33.50
500-525	$35.00
526-550	$36.50
551-575	$38.00
576-600	$39.50

For documents over 600 pages, add $1.50 for each additional 25 page increment.

PPPL--1660

DE82 013994

SOFT X-RAY MEASUREMENTS FROM THE PDX TOKAMAK

E. H. Silver, M. Bitter, K. Brau, D. Eames, A. Greenberger,

K. W. Hill, D. M. Meade, W. Roney, N. R. Sauthoff, S. von Goeler

Plasma Physics Laboratory, Princeton University

Princeton, New Jersey 08544 USA

ABSTRACT

Temporally and spatially-resolved profiles of the PDX soft X-ray spectra have been measured during single tokamak pulses of circular and divertor plasmas with a recently developed pulse height analyzer. This detection system incorporates an array of five vertically displaced sets of lithium-drifted silicon detectors, each consisting of three independent channels optimized for rapid data collection in adjacent energy regions. Simultaneous measurement of X-ray emission integrated along five chords of the plasma cross section can thereby be achieved. Abel inversion of these data yields temporally-resolved radial profiles of the local electron temperature from the slope of the continuum, concentrations of high-Z impurities from the characteristic line intensities, and a measure of Z_{eff} from the continuum intensity. The techniques of X-ray pulse height analysis, with illustrations featuring the results from the initial PDX circular plasma experiments are discussed in detail. In addition, comparisons between circular and divertor plasmas on PDX, derived from the X-ray measurements, are also presented.

1. INTRODUCTION

It is well known that radiative cooling by low- and high-Z impurities accounts for a significant fraction of the power loss from tokamak plasmas. Several investigators have shown that high-Z impurity radiation can seriously impair tokamak performance [1,2,3], and they have provided motivation for the impurity control experiments already begun at several laboratories. As plasma electron temperatures rise with the continued development of large tokamaks, a greater fraction of the total radiation is shifted toward higher energies. The study of soft X rays emitted between 1-20 keV has therefore increased in importance, furnishing electron temperature data and a wealth of impurity information. In particular, absolute intensity measurements of the soft X-ray continuum and characteristic emission lines lead to knowledge of the low- and high-Z impurity concentrations, respectively, and the slope of the continuum yields the plasma electron temperature.

The determination of radial profiles of these plasma parameters from the X-ray data involves spectral measurements along several plasma chords. Prior to the operation of PDX this required many tokamak pulses since the most advanced X-ray detection systems were capable of viewing only along a single plasma chord during one shot [4-9]. The irreproducibility of tokamak discharges subjected the resulting radial profiles to large uncertainties. In this article we report on the first time-resolved spatial profiles of the soft X-ray spectra acquired during single pulses of the PDX tokamak. These data were obtained with a recently developed X-ray pulse height analyzer, the design and operation of which is described in detail in Section 2 and associated appendices. The theory of X-ray production, applicable to this experiment, is reviewed in Section 3, and the impurity analysis, together with results that typified the initial circular plasma experiments conducted in April 1979 on PDX, is discussed at length in Section 4. January 1980 marked

the commencement of impurity control studies with the Poloidal Divertor on PDX. Comparisons between circular and divertor plasmas, derived from the X-ray measurements, are presented in Section 5.

2. INSTRUMENT

The pulse height analyzer designed for the PDX tokamak, shown schematically in Fig. 1, incorporates an array of five vertically displaced sets of lithium-drifted silicon detectors, each consisting of three independent channels. The five detector sets, which are connected to the vacuum vessel by five 3 m long stainless steel tubes that pivot vertically near the entrance to the vacuum vessel, provide the capability to simultaneously measure the X-ray emission integrated along five chords of the plasma cross section; assuming some symmetry for the emission, radial profiles can then be calculated using Abel inversion techniques. This multi-detector scheme eliminates the detrimental effects of shot to shot fluctuations in plasma conditions associated with earlier detection configurations which were dependent upon the movement of a single detector to view different regions of the plasma.

Each detector set consists of three Si(Li) crystals mounted side by side behind 0.0005 inch beryllium windows which are integral parts of a single vacuum enclosure. Each crystal has an active area of $10mm^2$ and is most sensitive between 1.5 keV and 27 keV. These low and high energy cutoffs represent points where X-ray detection efficiency is 67%. Detector efficiency drops significantly at low energies because of X-ray absorption by the window material. At photon energies greater than 27 keV, the probability that X rays are absorbed within the finite depth (3.73 mm) of the crystal is reduced and impairs the energy response.

A detector views the plasma through a series of lead collimators placed at several locations inside the 3 m tube (see Fig. 2.). These are conical in shape (smaller diameter hole closest to detector) to reduce the intensity of fluorescence. The X-ray intensity recorded by the detector is remotely

controlled by an interchangeable set of apertures placed at the entrance to the tube. These apertures provide a dynamic range in count rate of 1:400, furnishing the versatility needed to accommodate variations in plasma conditions encountered in tokamak discharges. Each collimating tube includes an X-ray source consisting of a biased filament and targets of Al, Ti, and Cu for energy calibration of the complete detector-electronics chain. Ceramic breaks electrically isolate the detectors from the tokamak and supporting structures and, together with iron rings that surround the detectors, minimize magnetic pickup in the form of eddy currents. Furthermore, lead shields prevent the penetration of hard X-ray radiation originating at the plasma limiter; hard X-ray-induced Compton-electrons would otherwise lower the X-ray signal to background ratio in certain discharges containing a significant population of high energy electrons called "runaways."

The finite duration of the tokamak pulse demands that the data collection rate of the detection system be maximized in order to minimize statistical uncertainties. High count rates, however, increase the probability that two photons will arrive "simultaneously," producing false double pulses. This "pulse pileup" distorts the x-ray spectrum, particularly at high energies where the true photon intensity is already appreciably low due to the sharp exponential fall-off of the spectrum with increasing energy (Fig. 3). An arbitrary photon spectrum, $S(E)$, is deformed by including pileup to a distorted spectrum, $S_M(E)$, which can be written as

$$S_M(E)dE = S(E)dE - 2S(E)R_T \tau \, dE + \tau \, dE \int_{E_{min}}^{E-E_{min}} S(E')S(E-E')dE' \qquad (2.1)$$

where E is the photon energy, τ the pulse pair resolution of the amplifier pileup rejector, E_{min} the low energy limit of detector sensitivity, and $R_T = \int_{E_{min}}^{\infty} S(E)dE$. This expression for $S_M(E)$ assumes that the maximum amplitude of two pulses add when they are separated in time by an interval, τ, an approximation that slightly overestimates the effects of pileup. The reader is referred to Appendix A for more details including a derivation of Eq. (1.1).

Pulse pileup induced spectral distortion is reduced with our triple-crystal detector arrangement. A set of properly chosen beryllium and aluminum filters are remotely positioned in front of the three detector channels, creating three adjacent energy bands (see Fig. 3). The detector channel behind the thinnest foil measures the low energy spectrum. The second and third channels both measure the high energy region where pileup occurs in the first channel. Each set of 3 foils is designed to allow for roughly 400 eV variations in plasma temperature that may occur during a pulse. To obtain the same count rate and statistical accuracy in the three channels, a lead aperture of appropriate size is positioned between each filter-crystal pair; the smallest diameter hole is associated with the thinnest foil and the hole with the largest area is placed behind the thickest foil. Appendix B describes the technique of foil and aperture selection.

A tradeoff must be made between a detector's energy resolution and data collection rate capabilities for all photon counting techniques. The PDX pulse height analyzer normally measures X rays at count rates of 20-35 kHz, using a 1 μsec amplifier shaping time constant while maintaining an energy resolution FWHM of 230 eV for 6 keV photons.

The arrangement of electronics is shown in Fig. 4. The function of the analog components illustrated in Fig. 4 is well-known [10], but the data

storage electronics merit a brief discussion. Temporal evolutionary studies of a plasma discharge that typically lasts for 1 sec require the acquisition of a spectrum at least every 60 msec. This collection time interval is generally sufficient to obtain statistical accuracy while providing a time history of the pulse. To accommodate this quantity of information, the pulse height system incorporates a modular network of 15, 4K memories; 16 groups can be stored in each memory by operating the ADC with a conversion gain of 256.

When a tokamak pulse begins, a machine-generated trigger initiates a programmable real-time clock which sequences the data acquisition hardware. During the prescribed collection time interval preset remotely by the computer, the digitized data from the 15 detector channels is transferred from the individual ADCs to the first 256 word segment of the 4K memories via the multiplexor/router. At the end of the time interval, the real-time clock issues a trigger and resets. For subsequent clock cycles, the multiplexor/router directs the data into successive 256 word memory partitions until the memory for each detector channel is filled (the starting address for each partition is [256 x (No. of time group -1)]). Additionally, scalers record the total input count rate (which is larger than or equal to the output count rate because of pile-up rejection) from an amplifier with a very short time constant (~ 0.4 μsec) for the 16 integration time groups. The measured spectral intensity can then be scaled to account for the dead time of the system.

Following a tokamak pulse, the data collected by the three channels are synthesized by correcting each raw spectra for the particular filter attenuation, channel efficiency, dead time, and geometry. Synthesis of the data is fully outlined in Appendix C. Figure 5 depicts the synthesis of the three raw data channels into one spectrum.

3. THEORY

The X-ray intensity spectrum emitted by a hot plasma is characterized by a set of continua that fall off exponentially with increasing photon energy. Frequently, emission lines peculiar to impurity ions in the gas are visible above this continuum [11,12].

Bremsstrahlung and radiative recombination are the two dominant emission processes contributing to the continuous X-radiation. The former involves the scattering of a free electron by the Coulomb field of an ion causing the electron to make a transition from one free state to another while emitting a photon. Photon production by the latter radiation mechanism results from the capture of a free electron into a bound state of an ion.

The bremsstrahlung radiation rate can be expressed as

$$\frac{dP_{ff,ij}(T_e,E_\nu)}{dE_\nu} = 3 \times 10^{-15} n_e n_i \left(\frac{n_{ij}}{n_i}\right) Z_{ff_i}^2 T_e^{-1/2} \times \bar{g}_{ff}(T_e,E_\nu) \exp(-E_\nu/T_e) \quad [\text{keV}/(\text{keV-cm}^3\text{-sec})] \tag{3.1}$$

where $dP_{ff,ij}(T_e,E_\nu)$ is the power radiated into the photon energy interval dE_ν by an impurity ion, i, in a charge state, j, and n_e is the electron density. n_i is the total density of the i^{th} impurity element while the density ratio n_{ij}/n_i is the relative abundance of the j^{th} ionic charge state of the impurity, i. Z_{ff_i}, the effective positive charge of the ionic species, (ij), is chosen for simplicity to equal the nuclear charge, Z_{iN}, with the understanding that the lower energy bremsstrahlung intensity will be high by no more than 30%. A rigorous analysis may be found in the literature [13,14]. T_e and E_ν are the electron temperature and photon energy,

respectively, in keV, and $\bar{g}_{ff}(T_e,E_\nu)$ is the temperature averaged Gaunt factor which is near unity in most cases. This expression must be summed over all the ionic species (ij) present in the plasma to yield the total bremsstrahlung power.

The power due to radiative recombination can be approximated by

$$\frac{dP_{fb,ij}(T_e,E_\nu)}{dE_\nu} = 3 \times 10^{-15}\, n_e n_i \left\{ \frac{n_{ij}}{n_i} Z_{ij}^2\, T_e^{-1/2} \beta_{ij}(T_e,E_\nu) \exp\left(-\frac{E_\nu}{T_e}\right)\right\}$$

$$\text{keV/(kev-cm}^3\text{-sec)} \quad ;$$

$$\beta_{ij}\,(T_e,E_\nu) = \sum_n \frac{F_n}{n^3}\, \bar{g}_{fb}\,(T_e,E_\nu,n)\, \exp\left(\frac{I_{ij,n}}{T_e}\right) \exp\left(\frac{I_{ij,n}}{T_o}\right)$$

$$+ \sum_{\alpha=1} \frac{2}{(n+\alpha)} \frac{Z_{ij}^2\, I_H}{(n+\alpha)^2}\, \bar{g}_{fb}\,(T_e,E_\nu,n+\alpha)\, \exp\left(\frac{Z_{ij}^2\, I_H}{(n+\alpha)^2\, T_e}\right) \theta(E-I_{i,j,n}) \qquad (3.2)$$

where Z_{ij} is the charge of the ion (ij) before recombination and I_H and $I_{ij,n}$ are the ionization potentials of hydrogen and the valence shell n of the recombined ion's ground state, respectively. The first term for β represents recombination to the level n with F_n designating the number of available electron vacancies in shell n [4]. The summation over α expresses the contribution to recombination from the quantum states $(n+\alpha)^2 = I_{ij,n+\alpha}$. Since the energy of the photon is the sum of the kinetic and binding energies of the recombining electrons, the spectrum displays recombination steps or edges at the energies equal to $I_{ij,n+\alpha}$ with $\alpha = 0,1,2..$ etc., and is indicated by the step function $\theta(E-I_{ij,n})$.

Line radiation is the third important radiation mechanism occurring in a hot plasma. At photon energies greater than 1.5 keV, K, L, and M shell emission from high Z impurities is predominant. Calculation of the excitation cross sections for specific ionic charge states are quite complex. For the purposes of this experiment, computations by Cowan [15] have been utilized. These include the processes of electron impact excitation, dielectronic recombination, cascading following radiative recombination to levels other than an ion's ground state, and inner shell ionization. The contribution from the latter two is small, however. For the high Z impurities present in the PDX tokamak, only the Kα transitions are important to this experiment. The power radiated in Kα transitions by an impurity ion, i in a charge state, j can be expressed as

$$P_L(T_e)_{ij} = n_e n_i \left(\frac{n_{ij}}{n_i}\right) \langle \sigma v(T_e) \rangle_{ij} E_{K\alpha} \frac{\text{keV}}{\text{cm}^3\text{-sec}} \tag{3.3}$$

where $\langle \sigma v(T_e) \rangle_{ij}$ is the total excitation cross section averaged over a Maxwellian velocity distribution.

The relative abundance factors, n_{ij}/n_i, depend strongly upon the electron temperature, ion species ionization and recombination rates, particle transport, and particle confinement time. Calculations for astrophysical applications are generally based on the characteristics of a coronal plasma where particle transport and time dependent particle densities are judged to be unimportant. In this coronal equilibrium model, ionization balances recombination; i.e.,

$$n_{ij}\, \alpha_{ij}(T_e) = n_{ij-1}\, S_{ij-1}\, (T_e) \tag{3.4}$$

where α and S are the recombination and ionization rates, respectively. The premise that a discharge in a large tokamak is in coronal equilibrium is a somewhat simplified view but it appears to be a satisfactory approximation of plasma conditions for electron densities of $5 \times 10^{13} cm^{-3}$ and higher [2,16, 17]. The coronal model loses validity at lower densities, however, as the recombination times of highly stripped ions —— specifically those in helium-like states —— become greater than the particle confinement times [17]; plasma transport dominates in such situations. Further perturbations to equilibrium conditions occur during injection of neutral hydrogen or deuterium beams which increase the likelihood that charge exchange recombination will shift the ion charge distribution toward the less ionized species [18].

In most cases, the modification in charge state distribution due to charge exchange or plasma transport at low densities amounts to a shift by only one or two charge states. The resulting difference in excitation cross sections between neighboring ionic species within the temperature range of 0.4 keV and 2 keV is less than or equal to the uncertainties associated with the individual cross sections themselves [19].

Inasmuch as our radiation rate calculations are uncertain at this level, we assume that characteristics of a coronal plasma best describe the tokamak discharges, and we await the development of detailed non-equilibrium plasma models and more precise excitation cross sections.

4. IMPURITY ANALYSIS

Soft X-ray spectra measured with a pulse height analyzer provide a means to determine the electron temperature as a function of tokamak minor radius. Together with the electron density measured by microwave interferometry or laser scattering diagnostics, X-ray spectra also furnish sufficient information to obtain radial profiles of impurity concentrations and, hence,

Z_{eff}. Furthermore, every profile can be temporally resolved. In the following sections we discuss the data analysis performed on X-ray pulse height spectra measured during the initial circular plasma experiments of PDX conducted 1979 April and present the results of these calculations for typical discharge conditions.

4.1 Temperature

The PDX pulse height analyzer concurrently measures line integrated spectra from five plasma chords. Figure 6 typifies the spectra commonly obtained. [During initial experimentation of the PDX, only four of the five sets of Si(Li) detectors were operational, and their vertical positions were fixed.] The perpendicular distance from the plasma center to each chord is indicated in the lower left corner (i.e., 0, 12, 20, 30 cm).

To determine the localized electron temperature, the intensity of each line averaged spectrum, neglecting the impurity peaks, is fit to an exponential function with a 3rd order polynomial as argument. The coefficients of this polynomial are determined by the fit. The intensities calculated from these fits are Abel inverted at 10 different photon energies, generating spectra at local radial positions. The slopes of the continua yield the electron temperature profile while the intercepts at zero energy are used to deduce the continuum enhancement. A detailed treatment is found in Appendix D.

The radial temperature profile for these data is shown in Fig. 7a. The profile is somewhat broad, with a peak temperature of ≈1.5 keV at the plasma center, decreasing to 750 eV at a radius of 20 cm. The error bars represent the extremes of the 67% confidence contours derived from the nonlinear least squares fits to the slopes and zero energy intercepts of the Abel inverted continua. The 67% confidence contour for r = 0, showing the relationship

between the two correlated parameters, temperature, T_e, and continuum enhancement, ζ, is presented in Fig. 7b.

4.2 High-Z impurities

High-Z impurities, $14 < Z < 50$, emit characteristic Kα radiation within the sensitive energy range of the pulse height analysis system. The Si(Li) detector cannot, however, resolve the emission lines attributable to the different charge states of a particular element. Rather, the strength of an X-ray line visible above the continuum (see Fig. 6) is proportional to the collective intensities of the element's ionic species, a charge state distribution which is dependent upon electron temperature, plasma transport, and other recombination mechanisms as described earlier. Ignoring the latter two, Eq. (3.3) then becomes

$$P_L(T_e) = n_e n_i \langle \sigma v \rangle_{T_e, K\alpha} \cdot E_{K\alpha} \ \text{keV}/(\text{cm}^3\text{-sec}) \qquad (4.1)$$

where $\langle \sigma v \rangle_{Te, K\alpha}$ equals the sum of the individual charge state cross sections $\langle \sigma v(T_e,) \rangle_{ij}$ [14], weighted by the fractional abundance, n_{ij}/n_i, obtained from coronal equilibrium models [20,21,22]; the temperature is furnished from the continuum X-ray data. The cross sections for chlorine and titanium, high Z impurities peculiar to the PDX plasma, are shown in Fig. 8. These have been interpolated from values of $\langle \sigma v \rangle_{Te, K\alpha}$ calculated for iron and argon by Cowan [15]. It should be noted again that these data possess large uncertainties arising from variations in the charge state cross sections and coronal equilibrium calculations; results accurate to within a factor of 2 are not unreasonable. Once the elemental line intensities have been measured along several plasma chords, a radial profile of the X-ray power emitted by an impurity per unit volume of plasma can be computed by Abel inversion

methods. Substitution of these intensity values into Eq. (3.5) yields the desired high Z impurity concentrations.

Figures 9a, and 9b exhibit the time resolved radial profiles of the ClKα power derived from the spectra shown in Fig. 8. The presence of the chlorine in the plasma arises from cleansing the stainless steel vacuum components with HCl [23]; PDX employs titanium limiters, the source of the impurity which presumably generates copious TiKα X rays. The chlorine emission extends to at least 30-35 cm while the intensity of Ti X rays disappears between 20-30 cm. According to coronal equilibrium calculations, Cl^{14+}-Cl^{16+} and Ti^{12+}-Ti^{20+} are the dominant charge states present throughout the plasma. Using a parabolic electron density profile determined from a line averaged microwave interferometry measurement [24], typical Cl densities range between 0.01% - 0.03% (~3.75×10^{9} cm^{-3}) while Ti abundances are within 0.08% - 0.3% (~$3.75 \times 10^{10} cm^{-3}$) (see Figs. 9c,d). These values agree with spectroscopic measurements in the ultraviolet to within 25% [25]. It should be noted that the apparent off-axis peaking of the Ti density (Fig. 9c) is probably not significant; the radial Ti density profile is essentially flat to within the uncertainties of the experiment.

4.3 Low Z impurities

The X-ray continuum emitted by an impurity-filled plasma is more intense than that produced by a plasma of hydrogen. Measurement of this enhancement, ζ, together with a knowledge of the high Z abundances, provides sufficient information for computing the impurity content of low Z contaminants such as oxygen and carbon; these do not radiate emission lines within the sensitive bandwidth of the detector.

Comparing Eq. (3.2) with Eq.(3.1) indicates that the power radiated through radiative recombination by an individual charge state, j of an element, i can be expressed as

$$\frac{dP_{fb,ij}}{dE_\nu} = \frac{dP_{ff,ij}}{dE_\nu} [\gamma_{ij} - 1] \tag{4.2}$$

where $[\gamma_{ij} - 1]$ equals $\beta_{ij} \frac{z_{ij}^2}{z_{iN}^2}$.

The contribution to the total continuum from this single ion is then

$$\frac{dP_{TOT,ij}}{dE_\nu} = \gamma_{ij} \frac{dP_{ff,ij}}{dE_\nu}. \tag{4.3}$$

Summing this expression over all elements and their respective charge states known to be present in the plasma yields the complete expression for the continuous X-ray radiation from a hot plasma

$$\frac{dP_{TOT}}{dE_\nu}(T_e, E_\nu) = 3 \times 10^{-15} n_e^2 \sum_i \frac{n_i z_{iN}^2}{n_e} \sum_j \gamma_{ij} \frac{n_{ij}}{n_i} T_e^{-1/2} \tag{4.4}$$

$$\times \exp\left(\frac{-E_\nu}{T_e}\right) \frac{\text{keV}}{\text{keV-cm}^3\text{-sec}}.$$

γ_{ij}, which represents the enhancement of the recombination radiation over bremsstrahlung is plotted in Fig. 10 for titanium, chlorine, carbon, and oxygen. The sum over all charge states, j in Eq. (4.4) above, is obtained by again invoking a coronal equilibrium model which weights the γ_{ij} by the fractional abundances, n_{ij}/n_i. The effective $\bar{\gamma}_i = \sum_{ij} \gamma_{ij} n_{ij}/n_i$ that results for each ion is depicted by the dotted lines in Fig. 10.

Consequently, the ratio ζ of a spectral intensity that includes impurity contributions to one that is a product of hydrogen solely is

$$\zeta = \frac{\dfrac{dP_{TOT}(T_e,E_\nu)}{dE_\nu}}{\dfrac{dP_{ff}(T_e,E_\nu,Z=1)}{dE_\nu}} = \sum_i \bar{\gamma}_i \frac{n_i Z_{iN}^2}{n_e} = \left[n_p Z_p^2 + \sum_i \bar{\gamma}_i n_i Z_{iN}^2\right]/n_e \qquad (4.5)$$

where the subscript p represents the background plasma —— hydrogen, in all likelihood. Writing the electron density, n_e, as

$$n_e = n_p Z_p + \sum_i n_i \bar{Z}_i \qquad (4.6)$$

where $\bar{Z}_i = \sum_j (n_{ij}/n_i) Z_{ij}$ and substituting for n_p into Eq. (4.5) yields

$$\zeta = Z_p - Z_p \sum_i \frac{n_i}{n_e} \bar{Z}_i + \sum_i \bar{\gamma}_i \frac{n_i}{n_e} Z_{iN}^2 \,. \qquad (4.7)$$

Experimentally, ζ is easily determined from the relation

$$\zeta = \frac{I(E=0,T_e)\, T_e^{1/2}}{3 \times 10^{-15}\, n_e^2} \quad \text{where} \qquad (4.8)$$

$I(E=0,T_e)$ is the zero energy intercept of the Abel inverted continuum.

The low Z plasma constituents in PDX are primarily carbon and oxygen; a 30 Å carbon layer is usually present on all metal surfaces, and a residual oxygen content always seems to exist even after many hours of vacuum pumping [23]. Since there is insufficient X-ray information to determine uniquely their individual concentrations, the oxygen density can be calculated in terms of a presumed carbon density. The carbon to oxygen density ratio can therefore be defined as $R \equiv n_C/n_O$. Finally, the oxygen concentration can be written as

$$\frac{n_O}{n_e} = \frac{\zeta - z_p - \sum_{i\neq C,O} (\bar{\gamma}_i z_{iN}^2 - \bar{z}_i z_p)\, n_i/n_e}{-z_p \bar{z}_O + \bar{\gamma}_O z_O^2 - R z_p \bar{z}_C + R\bar{\gamma}_C z_C^2} \tag{4.9}$$

and

$$z_{eff} = \sum_i \frac{n_i z_i^2}{n_e} = \frac{n_O}{n_e}\left[R\bar{z}_C^2 + \bar{z}_O^2\right] + \frac{n_p}{n_e} + \sum_{i\neq C,O} \frac{n_i}{n_e} \bar{z}_i^2 \,. \tag{4.10}$$

The continuum enhancements for the spectra shown earlier range from $\simeq$ 8 at inner radii to $\simeq$ 35-40 at the outer edges of the plasma. The inferred average oxygen and carbon concentration for an R value of 1 is $\approx$ 1.5%, implying a z_{eff} $\approx$ 2.5 as shown by the radial profiles in Figs. 9e,9f.

More importantly, varying R over a wide range enables the X-ray measurements to predict the "limits" of the oxygen and carbon concentrations and, hence, z_{eff}. As an example, Fig. 11 depicts the ratio, R, effectively ranging between 0 and ∞, the extreme cases corresponding to a low Z content due only to oxygen or only to carbon. The contributions to the total z_{eff} at the plasma center, shown in the top curve, from oxygen, carbon, titanium, and chlorine are also depicted. The measured titanium and chlorine concentrations combined with the measured enhancement value thus imply that z_{eff} must fall between 2.5 and 3.2, a relatively narrow range by tokamak standards.

5. DIVERTOR-CIRCULAR PLASMA COMPARISON

To investigate methods of impurity control in high temperature plasmas and to test the effectiveness of poloidal divertors in particular, PDX has been equipped with a magnetic limiter. Two identical sets of four distinct poloidal field coils encircle the interior of the torus. These coils in

conjunction with titanium evaporators and titanium neutralizer plates comprise the magnetic limiter system. Energizing different pairs of coils shapes the plasma into one of three standard configurations, a D-shaped plasma, a square cross-section, or an inverse-D, as shown in Fig. 12.

The outer edge of the plasma, termed the "scrape off" region flows toward and around the activated coils and is neutralized at the neutralizer plates. This scrape off plasma is intended to sweep plasma particles toward the neutralizer plates; neutral impurity atoms ($Z > 2$) sputtered or evaporated from the vacuum vessel are expected to ionize in the scrape off layer and prevented from penetrating into the main plasma while central plasma ions diffusing outward are channeled away before striking the vacuum vessel wall. A more detailed discussion of the poloidal divertor may be found elsewhere [26].

Divertor plasmas were produced routinely in June 1980 and their impurity content compared with circular plasmas created under similar discharge conditions, i.e., identical major radius, plasma current, toroidal field, and similar electron density and temperature profiles. The titanium limiter was positioned at 42 cm for circular plasmas while the average separatrix radius of the inverted-D discharge was 38 cm. Most of the circular discharges were characterized by either sawtooth or m=1 MHD mode behavior and the two discharge types exhibited quite different radiation profiles. This behavior of the circular plasma together with erratic bursts of titanium influx in divertor discharges have complicated our systematic comparisons. However, substantial evidence, provided by X-ray and ultraviolet measurements [25], permit one to conclude that divertor plasmas are cleaner than the purest circular discharge. In addition, the divertor appears to be most efficient in reducing the high-Z impurity content while modestly reducing the low-Z concentration. The X-ray data is presented below.

Figure 13 depicts the electron temperature radial profiles for the three plasma cases measured at 500 ms into the discharges. The solid circle, open circle, and the x represent the divertor, m=1 circular, and sawtooth circular cases, respectively, and the solid curve fits each set of points equally well. Fig. 14 presents a comparison of the temporal profile of electron temperature at the plasma core. The similarities in the spatial and temporal behavior of electron temperature are clear and imply that the divertor-circular comparisons do not depend upon exact knowledge of impurity ion excitation cross-sections.

Radial profiles of electron density were not available for these experiments. The temporal behavior of the density was identical for the three plasma types [24]. Small variations in profile shape, i.e., flatness or peaking, cannot account for the dramatic shifts in radiated power detected by the X-ray PHA. As a consequence of this density and temperature behavior, the relative intensities of the Kα and continuum emission are direct indicators of shifts in impurity content from one discharge to another.

Fig. 15 compares the 2.8 kev Cl Kα X-ray emission from the plasma core of circular and divertor plasmas During the steady state portion of the pulse (at 500 ms of a 1 sec pulse) the X-ray intensity in the m=1 case is approximately ten times higher than in the circular sawtooth plasma, which in turn is roughly 10 times greater than the divertor discharge. Similarly, the titanium Kα radiation centered at 4.7 kev is 75 times higher in the plasma with m=1 activity than in a circular sawtooth plasma while the emission from a divertor discharge is another factor of 5 below that (see Fig. 16). Within the variations of electron temperature and density these findings provide strong evidence that high-Z impurity levels are lowest in the divertor discharges.

Further proof of this trend is furnished by comparing profiles of the X-ray continuum intensity weighted by $\sqrt{T_e(r)}$, i.e., $n_e^2 Z$ as given in Eq. (4.8). Fig. 17 clearly shows that the divertor plasma impurity level is at least a factor of 5 lower than the cleanest circular plasma. The profiles also indicate that the impurity content is peaked toward the plasma center in the m=1 discharge but relatively flat for the circular and divertor sawtooth plasmas. The low-Z impurity behavior can only be inferred from these continuum curves by first subtracting the high-Z contribution as discussed earlier in section 4. Table 5.1 lists these core plasma concentrations. The dominant impurities in the divertor plasma are oxygen and carbon since titanium and chlorine have been reduced by factors of six and ten, respectively, compared to the best circular discharge. Oxygen and carbon show a three-fold reduction. The m=1 circular discharge indicates an increase in all impurities, but the influx of titanium and chlorine is predominant.

6. SUMMARY

The PDX X-ray pulse height analysis system has demonstrated itself to be an extremely versatile diagnostic tool. Its capability to obtain time-resolved radial profiles from a single tokamak pulse permits one to contrast the measurements of electron temperature and impurity content from divertor and circular plasmas. Systematic comparisons of X-ray emission from discharges with and without a divertor have shown that a poloidal divertor reduces the overall plasma impurity content. In particular the concentration of high Z material is reduced by approximately an order of magnitude.

The authors would like to acknowledge R. Fonck, R. Hulse, D. Post, K. McGuire, K. Owens and G. Schmidt for helpful discussions. Special thanks to G. Bates, J. Boychuk, J. O'Sullivan, H. Feng, J. Gorman, W. Mycock, and T. Provost. Their invaluable technical assistance was essential to the completion of this experiment.

This work was supported by the U.S. Department of Energy Contract No. DE-AC02-76-CH03073.

TABLE 5.1

SOFT X-RAY ANALYSIS

Contributions to Z_{eff} in Core of PDX Plasmas

	Divertor (Sawtooth)		Circular (Sawtooth)		Circular (m = 1)	
$\bar{n}_e$ (10^{13} cm^{-3})	3.4		4.0		4.0	
	n_z/n_e	Z_{eff}	n_z/n_e	Z_{eff}	n_z/n_e	Z_{eff}
Chlorine	~ .001%	~ .002	.01%	.02	.07%	.15
Titanium	.001%	.004	.006%	.02	.1%	.4
Oxygen	0.1%	.06	.3%	.19	2%	1.28
Carbon	.06%	.02	.2%	.07	1.3%	.47
Hydrogen		.99		.96		.73
Z_x		1.08		1.3		3.0

Appendix A

PULSE PILEUP

The effects of pulse pileup can be modelled computationally; one straightforward approach is presented here. Given that a continuous spectrum of photons is emitted at an average rate, a, integrated over all energies, we write the combined probability that a photon (also termed "event") is not produced within a time interval, t, but does occur in a small time interval, dt, as

$$dP = ae^{-at}\,dt \quad . \qquad (A.1)$$

Equation (A.1) may also be interpreted as the probability that the time interval size between successive events falls within the range (t,t+dt). If N is a large number of successive intervals, the expression

$$n = N\int_{t_1}^{t_2} ae^{-at}\,dt = N\left[e^{-at_1} - e^{-at_2}\right] \qquad (A.2)$$

specifies the number of time intervals, n, that satisfy the requirements $t_1 < t_{D_i} < t_2$ where the t_{D_i}, i = 1,2,...n, are the individual durations of the n intervals [27]. If we let $t_1 = 0$ and set $t_2 = \tau$, the pulse pair resolution of the amplifier pile-up rejector, Eq. (A.2) becomes

$$n = N(1-e^{-a\tau}) \quad . \qquad (A.3)$$

Equation (A.3) states that the number of intervals between successive events with durations less than or equal to τ is n; it implies that pulse pileup will occur in the amplifier n times. For a large time $t \gg \tau$, the average rate of

photon production, a, is just N/t, and the total pulse pileup rate, a_p, is simply $a_p = a^2\tau$, expanding the exponential in Eq. (A.3) to first order in $a\tau$; we concern ourselves only with the pileup of two pulses, and therefore neglect higher order terms in the expansion. Referring to Figure A.1, the total measured rate, a_M, integrated over all energies and corrected for pileup is

$$a_M = a - a^2\tau \quad . \qquad (A.4)$$

We are more interested, however, in the perturbation of the spectrum as a function of energy and presently use Eq. (A.4) as the framework for deriving Eq. (1.1).

When the time interval between two photons of energies E_1 and E_2 is less than the amplifier pulse pair resolution, a new amplifier pulse corresponding to the pseudo-photon energy, $E_3 = E_1 + E_2$, is created.* The spectral distortion due to pulse pileup is therefore threefold; for each unreal photon added to the spectrum, two lower energy photons are lost. Since the total spectral rate, integrated over all energies must reduce to Eq. (A.4), we use the form of Eq. (A.4) to specify the three contributions to the measured rate, $S_M(E)$, within the energy range (E, E + dE). Assuming that the amplifier pulse heights of two photons add when they occur within the time interval, τ, the pileup production rate, $S_p(E)$, at energy, E from all photons with energies, E'<E is

* In this approximation the amplifier pulse shape is assumed to be square and tends to overestimate the pileup distortion. Dyer et al. [28] have improved upon this model by assuming that a triangular pulse shape better approximates the true Gaussian-like shape of the amplifier pulse.

$$S_p(E)dE = \tau\, dE \int_{E_{min}}^{E-E_{min}} S(E')S(E-E')dE' \qquad (A.5)$$

where E_{min} is the minimum energy detected by the system. Note that the integral of $S_p(E)dE$ over all energies is $a^2\tau$ where $a = \int_{E_{min}}^{\infty} S(E')dE'$.

Additionally, the loss of photons from the energy interval (E, E + dE) due to pileup can be shown to be

$$S_{LOSS}(E)\, dE = -2\tau S(E)dE \int_{E_{min}}^{\infty} S(E')dE' = -2\tau a S(E)dE \quad . \qquad (A.6)$$

The integral over all energies reflects the fact that a specific photon of energy, E, can pileup with another photon of any energy ,E', where $E_{min} < E' < \infty$. The effective pulse pair resolution time is 2τ since it does not matter which photon arrives first and accounts for the factor of two in Eq. (A.6). The final expression for the measured spectrum corrected for the energy dependence of pulse pileup is therefore

$$S_M(E)dE = S(E)dE - 2\tau\, S(E)dE\, a + \tau dE \int_{E_{min}}^{E-E_{min}} S(E')S(E-E')dE' \quad . \qquad (A.7)$$

APPENDIX B

CHOOSING APERTURES AND ABSORPTION FILTERS

In general, the detrimental spectral effects caused by pulse pileup can be reduced in three ways:

1) The measured spectrum can be modelled computationally in a manner similar to that presented in Appendix A; attempts to mathematically correct measurements for the count-rate-dependent pileup contribution can be made [28].

2) Experimentally maintain low count rates, limiting pileup to a minimum level.

3) Utilize filters to divide the spectrum into overlapping energy bands; each spectral segment is then measured by an individual detector. The width of each spectral segment extends to the energy beyond which the distortion due to pulse pileup is greater than some tolerable value; the distortion permitted clearly depends on the precision sought in the measurements. This pileup energy cutoff varies with filter thickness, count rate, and plasma temperature, and is established empirically by experiments and spectral simulations using Eq. (1.1).

The third method offers a way to measure directly the entire spectrum at high data rates without invoking mathematical corrections, and it has served as the basic framework for the PDX PHA design.

To simplify the following discussion, several parameters will be defined:

a) $E_{0.01}$ ≡ the energy at which filter transmission is 1%.

b) E_C ≡ the energy at which filter transmission is 37%.

c) $E_{P\#}$ ≡ the energy at which the effects of pileup distort the spectrum by # percent.

d) $A \equiv$ aperture area.

e) $R \equiv$ total integrated count rate recorded by a detector.

f) $T_e \equiv$ electron temperature.

g) $\mu_i(E) \equiv$ X-ray absorption coefficient of filter.

h) $X_i \equiv$ filter thickness.

i) $N(E) \equiv$ detector efficiency.

j) $T_{eH}, T_{eL} \equiv$ the high and low limits of the temperature range associated with a set of filters.

Following the technique outlined by method 3 above, the X-ray continuum emission transmitted by specific filters is simulated by a computer code. The intensity radiated as a function of energy and line averaged over twice the minor radius of the plasma is approximated by an equation of the form

$$I(E)dE = \frac{A}{E\,T_e^{1/2}}\left(1 + 1.5\,\frac{T_e}{E}\right)\exp\left[-\mu_i(E)X_i - E/T_e\right]dE\ \frac{\text{counts}}{\text{sec}}\ ; \qquad (B.1)$$

the factor $(1 + 1.5\ T_e/E)$ is an estimate of the profile effects associated with a measurement obtained along the central plasma chord.

By design, a group of three PHA filters must be chosen to transmit X-ray spectra from plasmas with electron temperatures that fluctuate by

ately 400 ev. This can be achieved with a minimum of pileup by requiring that transmission by at least two of the three filters be sufficient to produce a contiguous spectrum. The energy window of the filters must therefore satisfy several criteria. At T_{eH} of a specific temperature range, the low energy cutoff of the third (III) or high energy filter, $E^{III}_{0.01}$, must be less than $E^{I}_{p\#}$; $E^{I}_{p\#}$ is determined by computer simulations using Eq. (1.1) and an input spectrum, $S(E)$, defined by Eq. (B.1). Because of the steep exponential fall of the Maxwellian-type spectrum, detector II, which views the

plasma through a thicker foil than detector I, must be exposed to a larger volume of the source in order to maintain equal intensities in both detectors. Hence, fixed lead apertures with areas in the ratio of 1:40 are placed in front of detectors I and III, respectively. A filter of intermediate thickness ($E^{II}_{0.01} < E^{I}_{P\#}$) and aperture of intermediate size is placed in front of detector II.* As a result, detector II will record higher count rates by factors of three or four than those obtained by detectors I and II, but at $T_{eL} = T_{eH} - 400$ ev, the photon rates for II and I will be similar; the contribution from detector III will be reduced below I and II by a factor of 4 or 5.

Five overlapping temperature intervals have been established for the PDX PHA, and pulse pileup calculations have been performed to determine $E_{P\#}$ for every filter and, hence, the degree of overlap in each 3-filter group. Figure B.1 depicts the percent of spectral distortion that would stem from count rates of 10, 20, 40, 60, and 100 kHz as a function of the ratio, E/E_C for the five groups of filters. The distortion defined by these curves is illustrated in Fig. B.2. The solid line is a typical 1 keV continuum spectrum as it would be measured through a 0.030 in. beryllium filter at a 40 kHz count rate, assuming pulse pileup to be absent; the curve depicted by dashes of alternating sizes includes pulse pileup contributions, and the arrows define the degree of distortion between the two spectra. Notice, however, that the loss of low energy photons to the creation of pseudo high energy X rays, which is simply proportional to the total count rate [see Eq. (1.1)], introduces an intensity drop that is a constant fraction lower than the true spectrum. Consequently, the low energy portion of the measured spectrum has the

* The relative ratios between detectors I, II and III are 1:30:40, respectively.

identical shape as the true spectrum. Accounting for this negative departure in low energy intensity by extending the low energy spectrum upward in energy, assuming no pileup (curve with small dashes), effectively increases the degree of pulse pileup at higher photon energies. This is shown in Fig. B.2 by the arrows bridging the two different dashed lines.

The curves corresponding to a 10 kHz rate shown in Fig. B.1 imply that the energy ranges for three filters can be made to overlap and to sample a combined range of 6-10 keV, depending on temperature, while maintaining less than 2% pileup. In an attempt to remain conservative, but also to improve the counting statistics, we have accepted pileup distortion of 10%, thereby extending the allowable count rates to 40 kHz or 50 kHz.

As an example, the energy overlap of filters chosen to bridge the 0.6 keV to 1 keV temperature range is shown in Fig. B.3. It is assumed that at 1 keV detectors I and III both record spectra at 30 kHz. Their energy overlap begins at $E^{III}_{0.01} = 3.5$ keV and extends to the 10% pileup cutoff for detector I of $E^{I}_{P10} = 4.6$ keV. The total extent of the spectrum reaches $E^{III}_{P10} = 8.4$ keV. Detector II, which records approximately 100 kHz count rates, suffers from pileup anomalies that are greater than 10% and is neglected at this temperature. However, at a temperature of 0.6 keV, detectors I and II furnish the major contributions to the spectrum at count rate of 5.5 and 9 kHz, respectively, while the signal recorded by detector III is a factor of 5 or 8 lower: $E^{II}_{0.01} < E^{I}_{P10}$, so that we have sufficient overlap between the spectra of detectors I and II.

APPENDIX C

SPECTRAL SYNTHESIS

The final X-ray spectrum averaged across a plasma chord is synthesized from the data obtained by the three independent detector channels. The scaler outputs establish which spectral regions should be included with regard to problems of pulse pileup as stated in Appendix B. In addition, the scaler readings together with the pulse pair resolution time, τ, of the amplifier determine the dead time correction used to scale the raw data; the term "raw data" is used to represent the contents of the 256 energy bins of each memory subsection. The ratio between the total accumulated data in the 256 energy channels to the scaler counts is less than unity because of the system dead time. This fraction, f, can be written as,

$$f \simeq \frac{R_{scaler}}{R_M} (1 + R_{scaler}\,\tau) , \qquad (C.1)$$

where R_{scaler} is the count rate recorded by the scalers, and R_M is the raw data count rate.

The spectrum incident on each detector is therefore

$$R(E)_{plasma} = C[R_M(E)/n(E)]\, f\beta(E/\Delta E) \exp[\mu(E)x] \text{ kev/(kev-cm}^2\text{-sec)} \qquad (C.2)$$

where $R_M(E)$ has units of counts/sec, $\exp(\mu(E)x)$ corrects the rate for the filter attenuation [29,30], ΔE is the energy width of one of the 256 ADC

channels, $\eta(E)$ is the efficiency of the detector which depends on its window and crystal absorption at energy E, and β corrects the count rate for the reduction due to the solid angle subtended by the plasma volume at the detector. Specifically,

$$\beta = \left[\frac{A_D A_P}{4\pi D^2}\right]^{-1} \qquad (C.3)$$

where A_p is the area of the remotely controlled entrance aperture, A_D is the effective area of the detector (meaning the size of the small rear lead aperture, as discussed previously in Appendix B), and D is the distance between the front and rear apertures. Once the three measured spectra have been appropriately scaled, they are averaged according to their statistical weight to create one complete spectrum (see Fig. 5).

APPENDIX D

ABEL INVERSION

Radial intensity profiles of X-ray continuum and line radiation contain electron temperature and impurity concentration information. Such radial emission distributions in sources with circular cross sections can be computed using Abel inversion techniques [31,32], and their application to the PDX X-ray PHA measurements are discussed below. The reader is referred to the literature for several methods that have been developed to treat noncircular cross sections [33,34].

Calculating the localized electron temperature involves a fit of the intensity of each line averaged spectrum, $I_y(E)$, neglecting impurity peaks, to an exponential function of energy, E:

$$I_y(E) = P_{0,y}\exp(P_{1,y}E + P_{2,y}E^2) \text{ Kev/(cm}^2\text{-sec)} \qquad (D.1)$$

where y is the perpendicular distance from the plasma center to each chord, i.e., y = 0, 6, 12, 20, 30 cm, etc. (see Fig. D.1).

The $I_y(E)$'s are subsequently fit to an exponential function of the perpendicular distance, y, for ten different energies, 1<E<20 Kev:

$$I_E(y) = \exp[A_{0,E} + A_{1,E}y^2 + A_{2,E}y^3] \text{ Kev/(cm}^2\text{-sec)} . \qquad (D.2)$$

The $I_E(y)$'s are Abel inverted in order to generate the sources of emission, $\varepsilon(r,E)$ at localized radial positions:

$$\varepsilon(r,E) = \frac{-1}{\pi r}\frac{d}{dr}\left[\int_r^a \frac{I_E(y)\, y\,dy}{(y^2-r^2)^{1/2}}\right] \text{ Kev/(cm}^3\text{-sec)} \qquad (D.3)$$

where a is the minor radius of the plasma.

The slopes of the resulting continua formed by the sets of $\varepsilon(r,E)$ at specific radii yield the electron temperature profile while the intercepts at zero energy are used to deduce the continuum enhancement, ζ.

The high Z impurity intensity profiles are computed in a similar manner. The factor, $I_E(y)$, in Eq. (D.3) is simply replaced by the line averaged intensity of the particular impurity measured at each chordal position, y. Abel inversion is then a straightforward operation.

REFERENCES

[1] MEADE, D., Nucl. Fusion 14 (1974) 289.

[2] JENSEN, R.V., et al., Nucl. Fusion 17 (1977) 1187.

[3] ARUNASALAM, V., et al., Proceedings of the Eighth European Conference on Controlled Fusion and Plasma Physics, Vol. II, Prague, (1977).

[4] VON GOELER, S., et al., Nucl. Fusion 15 (1975) 301.

[5] SESNIC, S., IPP III/22 April 1976.

[6] EQUIPE TFR, Nucl. Fusion 17 2 (1977) 213.

[7] RICE, R., et al., private communication.

[8] GILL, R., et al., Nucl. Fusion 19 (: 9) 1003.

[9] DYER, G.R., private communication.

[10] MILLMAN, J., and TAUB, H., Pulse and Digital Circuits, McGraw-Hill Book Company, New York (1956).

[11] TUCKER, W.H. and KOREN, M., Astrophysical Journal 168, (1971) 283.

[12] BRUSSAARD, D.J., and VAN DE HULST, H.C., Rev. Mod. Phys., 34 (1962) 507.

[13] WEINSTOCK, R., Phys. Rev. 61 (1942) 584.

[14] LEE, C. M., PRATT, R. H., and TSENG, H. K., Phys. Rev. A 16 (1977) 2169.

[15] COWAN, R., private communication.

[16] HILL, K., et al., Phys. Rev. A 19 (1979) 4.

[17] BITTER, M., et al., Third APS Topical Conference on High Temperature Plasma Diagnostics, (March, 1980) 84.

[18] HULSE, R.A., POST, D.E., and MIKKELSON, D.R., Princeton Plasma Physics Laboratory, PPPL-1633, (March, 1980).

[19] VON GOELER, S., Diagnostics for Fusion Experiments Pergamon Press, Oxford and New York, (1979).

[20] JORDAN, D., Mon. Not. R. Ast. Soc. 142 (1969) 501, and Mon. Not. R. Ast. Soc. 148 (1970) 17.

[21] BRETON, C., DE MICHELIS, C., FINKENTHAL, M., and MATTIOLI, M., Fontenay-aux-Roses, Rep. Eur-Cea-Fc-948 (1978).

[22] POST, D.E., and JENSEN, R.V., Atomic Data and Nuclear Tables, Vol. 20, No. 5, (1977).

[23] DYLLA, H. F., private communication.

[24] SCHMIDT, G., private communication.

[25] FONCK, R., private communication.

[26] OWENS, D.K., et al., Journal of Nuclear Materials 93 & 94 (1980) 213.

[27] EVANS, R.D., The Atomic Nucleus (1955) McGraw-Hill, New York.

[28] DYER, G.R., et al., Nucl.Inst. and Methods, 161, (1979) 365.

[29] BRIGGS, F., and LIGHTHILL, R., Analytical Approximations for X-Ray Cross Sections II, SC-RR-710507, Sandia Laboratories, December, 1971.

[30] McMASTER, W.H., KERR DELLA-GRANDE, N., MALLETT, J.H., and HUBBELL, J.H., Compilation of X-Ray Cross Sections, UCRL-50174, Sec. II, Rev. 1, Lawrence Livermore Laboratory, May, 1969.

[31] BARR, W., Journal of the Optical Society of America, Vol. 52, No. 8, (1962).

[32] BOCKASTEN, K., Journal of the Optical Society of America, Vol. 51, No. 9, (1961).

[33] SAUTHOFF, N.R., and VON GOELER, S., IEEE Transactions on Plasma Science, Vol. PS-7, No. 3, (1971).

[34] SILVER, E., and RONEY, W., IEEE Transactions on Plasma Science, Vol. PS-8, No. 3, (1980).

FIGURE CAPTIONS

1. Schematic of the multi-detector PHA system designed for PDX.

2. Detailed view of one pulse height analyzer tube assembly.

3. Schematic illustrating how multi-detector PHA systems avoid problems with pulse pileup; the energy region where pileup occurs in detector I is measured with detector II.

4. Block diagram of PDX PHA electronics.

5. Raw data obtained by the three detectors are synthesized into one X-ray spectrum.

6. Typical spectra obtained from simultanous measurements along four plasma chords. The smooth curves represent polynomial fits to the continuum, neglecting the ClKα, TiKα, and TiKβ impurity peaks.

7. a) Electron temperature profile for the line integrated spectra shown in Fig. 6. The error bars represent the extremes of the 67% confidence contours; b) The 67% confidence contour for the radius R = 0 is depicted here.

8. Temperature averaged excitation cross sections $\langle\sigma v\rangle$ for the Kα emission of ions in coronal equilibrium. The FeKα values are based upon calculations made by Cowan [11] from which the ClKα and TiKα values have been interpolated.

9. Typical time resolved spatial profiles of several measured quantities; a-b) ClKα and TiKα radiated power; c-d) ClKα and TiKα impurity densities; c-f) oxygen impurity density and Z_{eff} for $n_C/n_O=1$.

10. Recombination enhancement factor, γ, is plotted vs electron temperature, T_e, for carbon, oxygen, chlorine, and titanium ions.

11. The contribution made by carbon, oxygen, titanium, and chlorine to Z_{eff} plotted as a function of the carbon-oxygen ratio n_C/n_O.

12. PDX Plasma Configurations.

13. Electron temperature profiles obtained at 500 ms into the pulse of a circular discharge with m=1 MHD activity (open circle), a circular plasma with sawtooth behavior (x), and a divertor discharge with sawtooth oscillation (closed circle).

14. Temporal behavior of electron temperature at core of three different plasma types.

15. Power radiated by chlorine Kα X-rays from core of PDX plasma. Circular and divertor discharges are compared.

16. Power radiated by titanium Kα X-rays from core of PDX plasma. Circular and divertor discharges are compared.

17. Radial profiles of X-ray continuum emission from divertor and circular plasmas.

A.1 A time series of photons occurring at an average rate, a.

B.1 The spectral distortion expected from count rates of 10, 20, 40 and 100 kHz is plotted as a function of E/E_C for the absorption filters utlized in the PDX PHA. The individual graphs are designated by the filter type and thickness; the energies where transmission is 1% ($E_{0.01}$) and 37% (E_C) are also indicated. These plots are organized in groups of six; each horizontal row demonstrates the energy overlap of the set of three filters; each set is categorized vertically by the high and low limits of their useful electron temperature range.

B.2 An illustration of spectral distortion. The solid line depicts a typical X-ray continuum for an electron temperature of 1 keV as it would be measured through a 0.030 in. beryllium filter at a 40 kHz count rate, assuming pileup to be absent. The large dashed line includes pulse pileup contributions, and the arrows define the degree of distortion plotted in Fig. B.1. The low energy portion of the pileup spectrum has the same shape but less intensity than the true spectrum. The smaller dashed line is a continuation of the low energy spectra with pileup, and the arrows bridging this curve with the solid curve indicates the extent to which the negative departure in intensity effectively increases the degree of pileup at high energies.

B.3 Energy overlap of the foil transmission curves for detectors I, II, and III at temperatures of a) 1 Kev and b) 0.6 Kev.

D.1 Geometrical configuration for Abel inversion of a circular cross section.

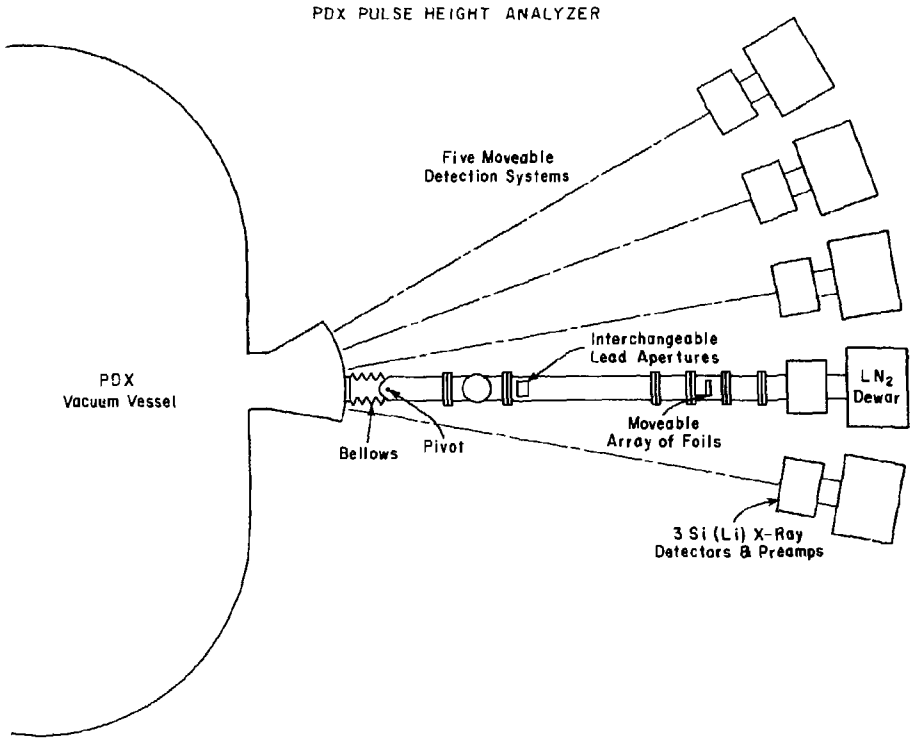
PDX PULSE HEIGHT ANALYZER
Five Moveable
Detection Systems
Interchangeable
Lead Apertures
PDX
Vacuum Vessel
LN_2
Dewar
Moveable
Array of Foils
Bellows
Pivot
3 Si (Li) X-Ray
Detectors & Preamps

Fig. 1

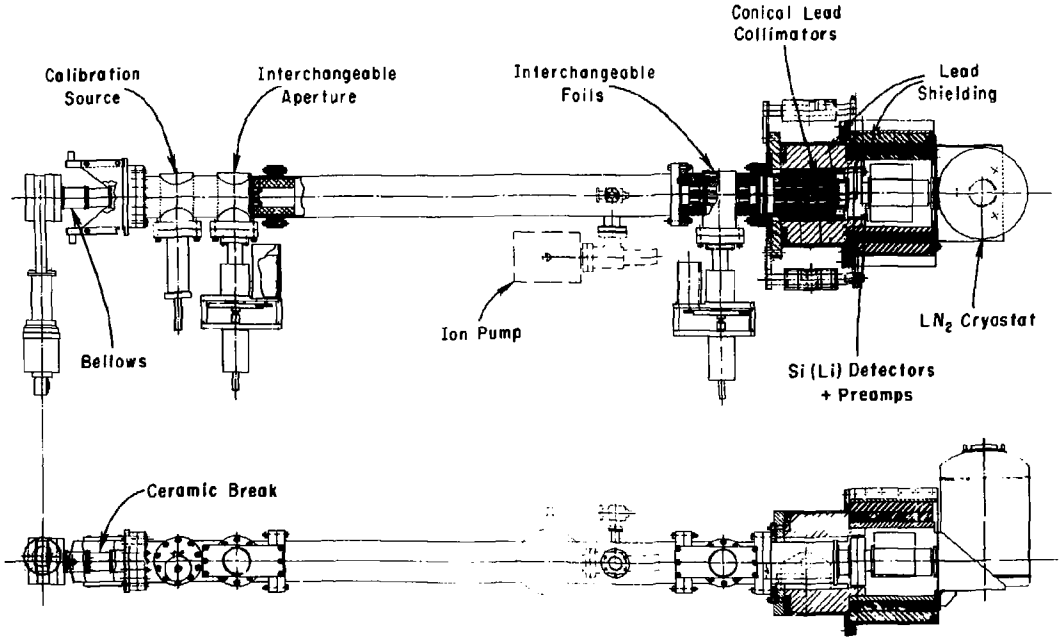
Conical Lead
Collimators
Calibration
Source
Interchangeable
Aperture
Interchangeable
Foils
Lead
Shielding
Ion Pump
Bellows
LN_2 Cryostat
Si(Li) Detectors
+ Preamps
Ceramic Break

Fig. 2

81X0018

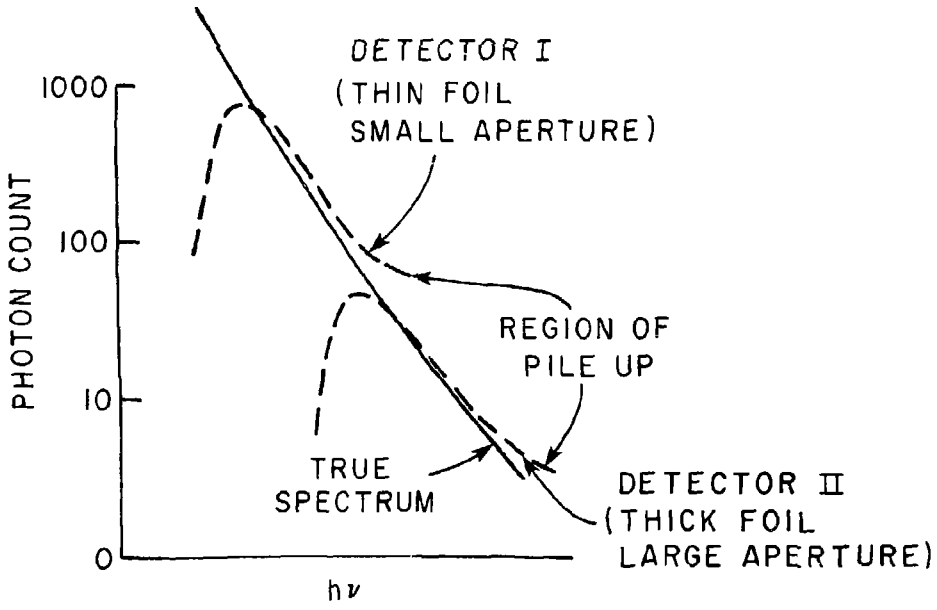

Fig. 3

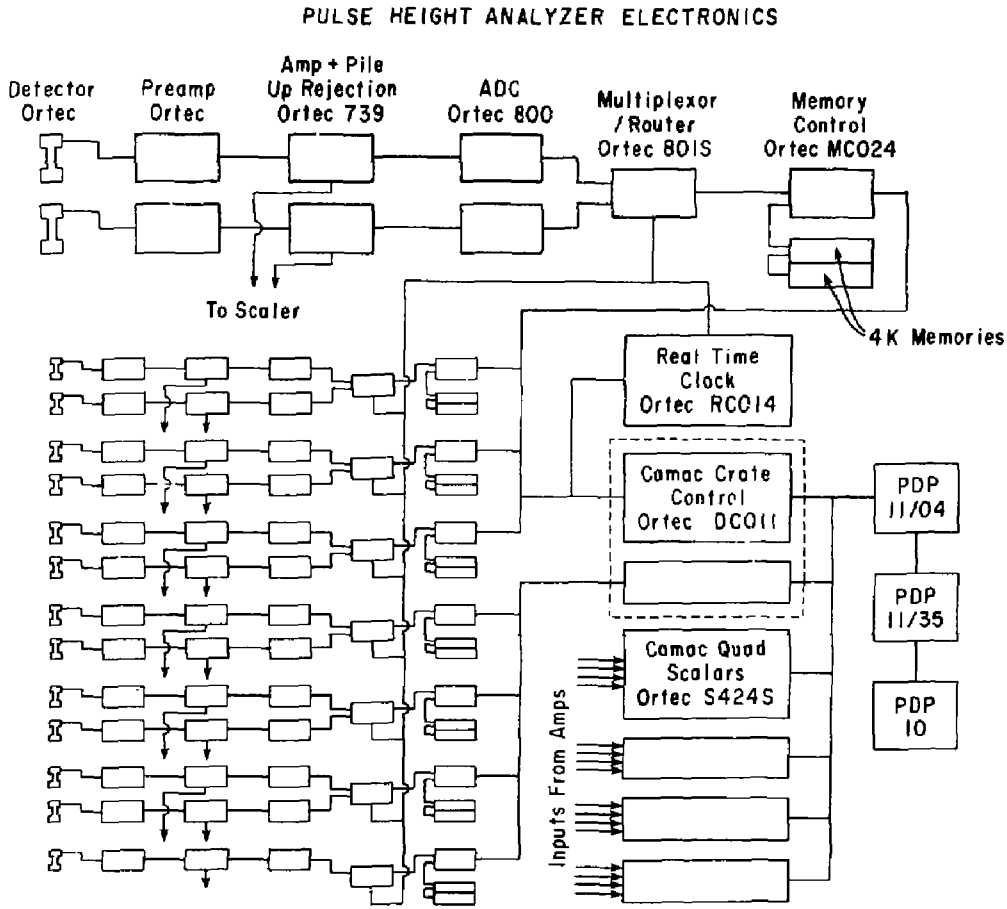
PULSE HEIGHT ANALYZER ELECTRONICS
Detector Ortec
Preamp Ortec
Amp + Pile Up Rejection Ortec 739
ADC Ortec 800
Multiplexor / Router Ortec 80IS
Memory Control Ortec MC024
To Scaler
4K Memories
Real Time Clock Ortec RC014
Camac Crate Control Ortec DC011
PDP 11/04
PDP 11/35
PDP 10
Camac Quad Scalars Ortec S424S
Inputs From Amps

Fig. 4

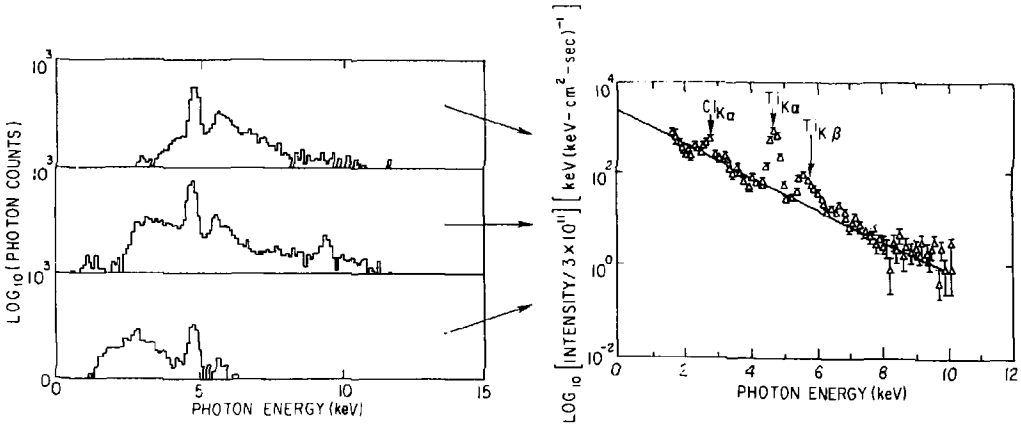
LOG10 [PHOTON COUNTS]
PHOTON ENERGY (keV)
LOG10 [INTENSITY/3×10^11] [keV(keV-cm^2-sec)^-1]
Cl Kα
Ti Kα
Ti Kβ
PHOTON ENERGY (keV)

Fig. 5

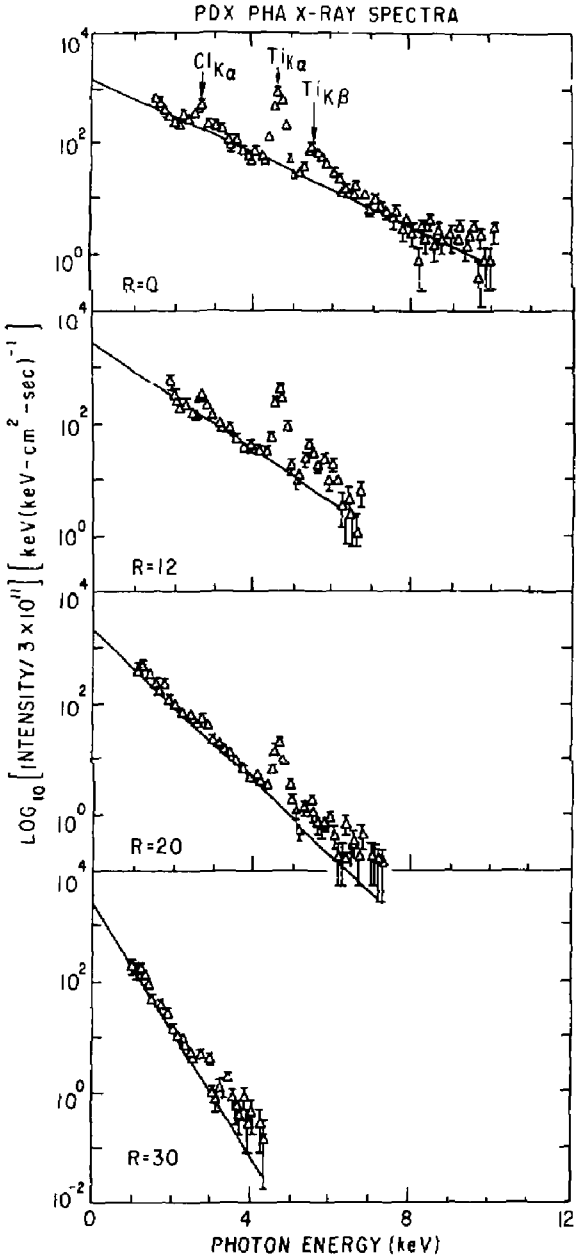
PDX PHA X-RAY SPECTRA
Cl Kα
Ti Kα
Ti Kβ
R=0
R=12
R=20
R=30
LOG10 [INTENSITY/ 3 x 10^11] [keV(keV-cm^2-sec)^-1]
PHOTON ENERGY (keV)

Fig. 6

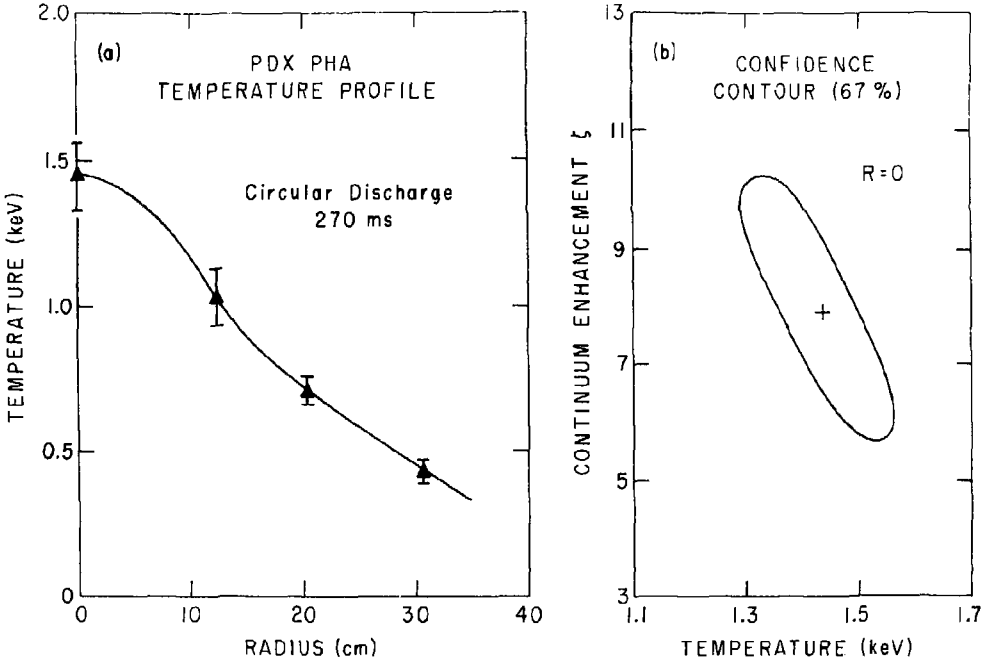
(a)
PDX PHA
TEMPERATURE PROFILE
Circular Discharge
270 ms
TEMPERATURE (keV)
RADIUS (cm)
2.0
1.5
1.0
0.5
0
0
10
20
30
40
(b)
CONFIDENCE
CONTOUR (67 %)
R=0
CONTINUUM ENHANCEMENT ξ
TEMPERATURE (keV)
13
11
9
7
5
3
1.1
1.3
1.5
1.7

Fig. 7

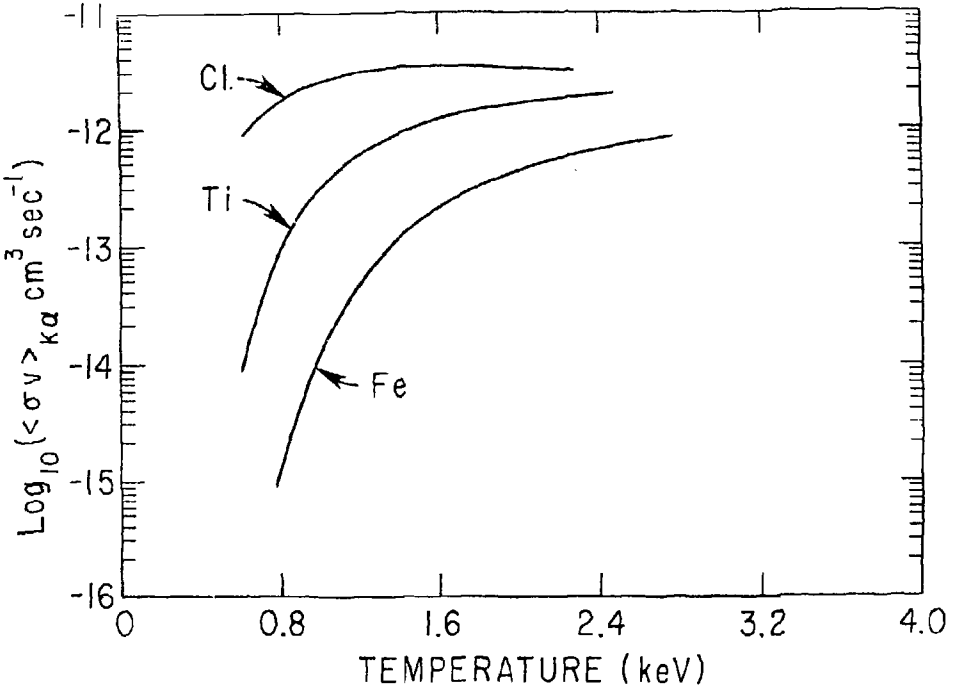
-11
-12
-13
-14
-15
-16
Cl
Ti
Fe
$Log_{10}(<\sigma v>_{K\alpha}\ cm^3\ sec^{-1})$
0
0.8
1.6
2.4
3.2
4.0
TEMPERATURE (keV)

Fig. 8

#8110020

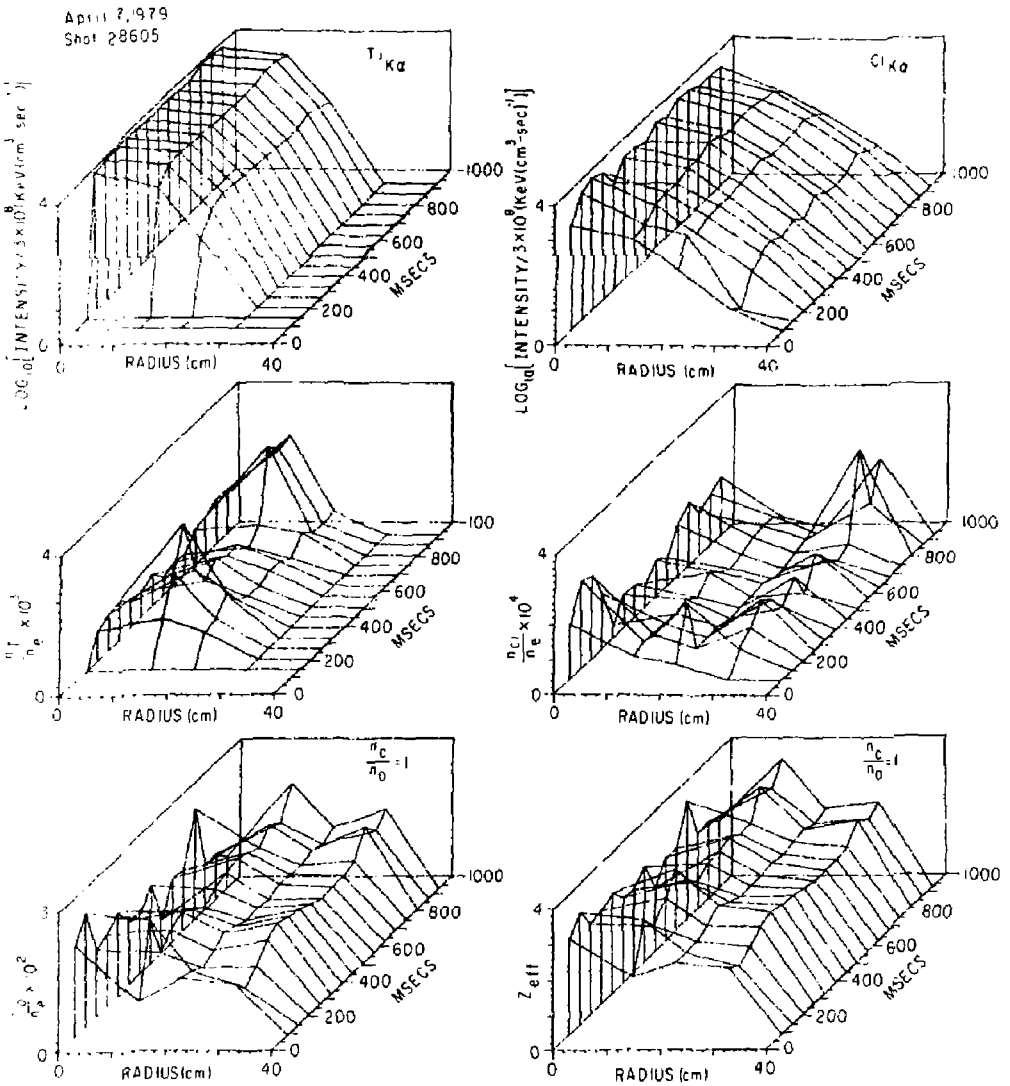

Fig. 9

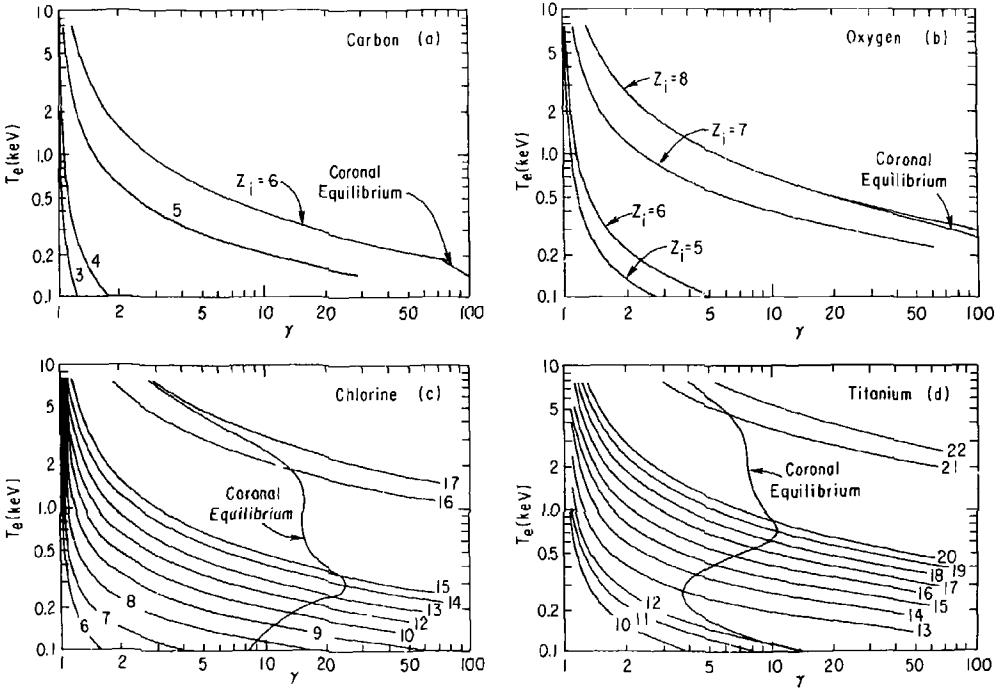
Carbon (a)
Oxygen (b)
Chlorine (c)
Titanium (d)
T_e(keV)
γ
Z_i=6
Z_i=7
Z_i=8
Z_i=5
Coronal Equilibrium
3
4
5
6
7
8
9
10
11
12
13
14
15
16
17
18
19
20
21
22

Fig. 10

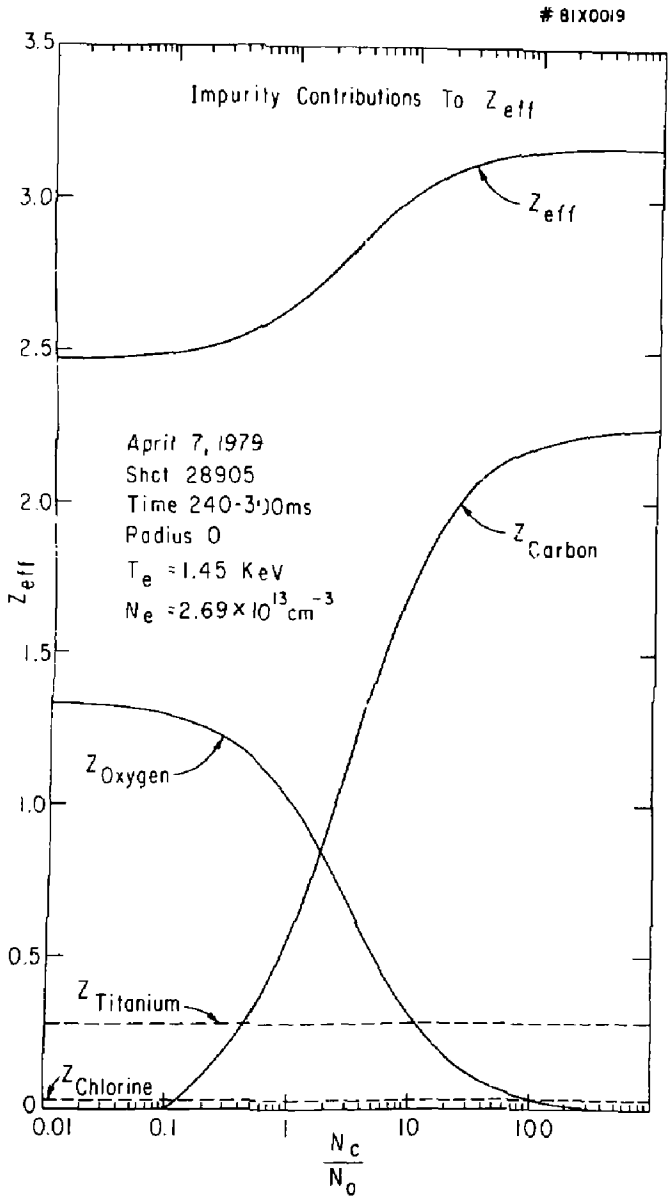
81X0019
Impurity Contributions To Z_{eff}
Z_{eff}
April 7, 1979
Shot 28905
Time 240-300ms
Radius 0
T_e = 1.45 KeV
N_e = 2.69 × 10^{13} cm^{-3}
Z_{Carbon}
Z_{Oxygen}
$Z_{Titanium}$
$Z_{Chlorine}$
Z_{eff}
3.5
3.0
2.5
2.0
1.5
1.0
0.5
0
0.01
0.1
1
10
100
$\frac{N_c}{N_o}$

Fig. 11

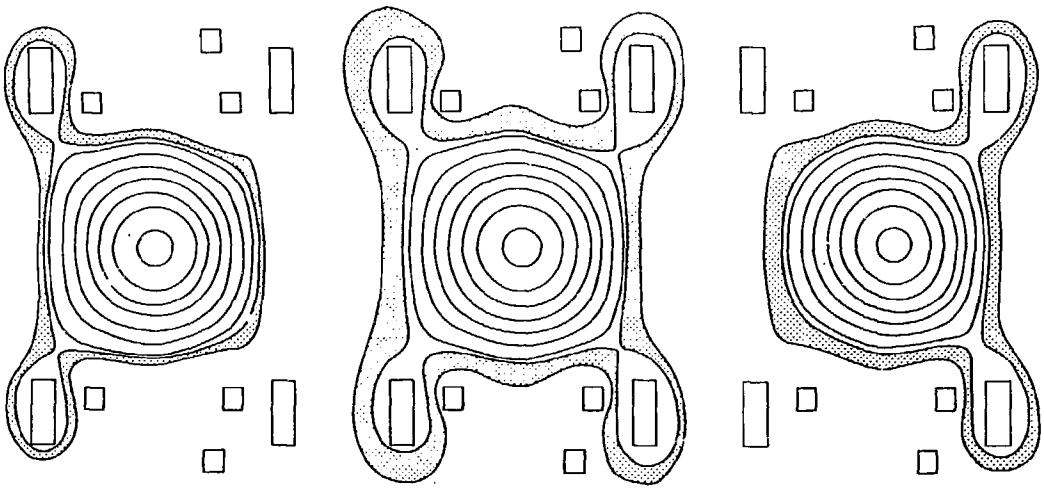

Fig. 12

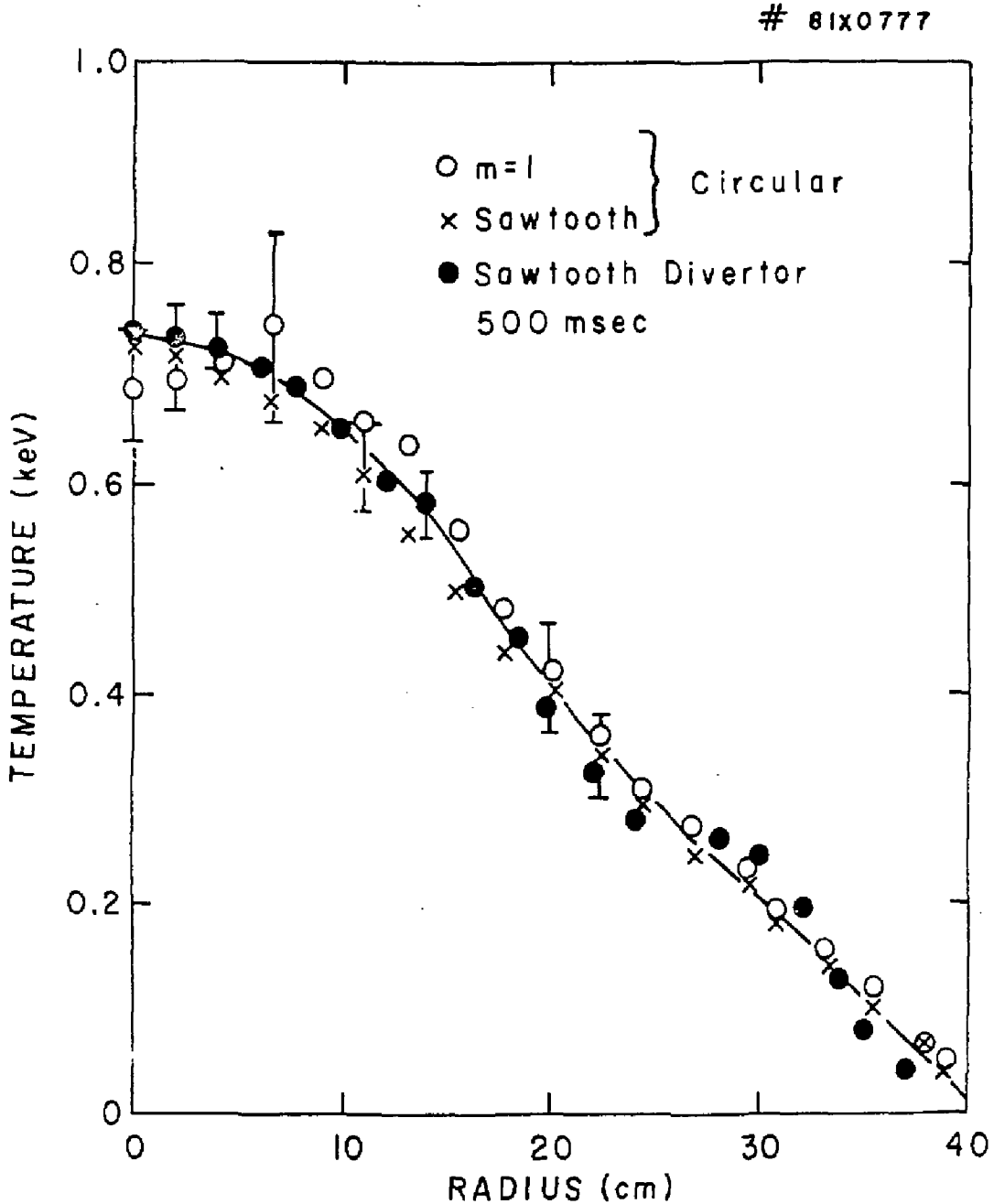
81X0777
1.0
0.8
0.6
0.4
0.2
0
TEMPERATURE (keV)
0
10
20
30
40
RADIUS (cm)
O m=1
× Sawtooth
Circular
● Sawtooth Divertor
500 msec

Fig. 13

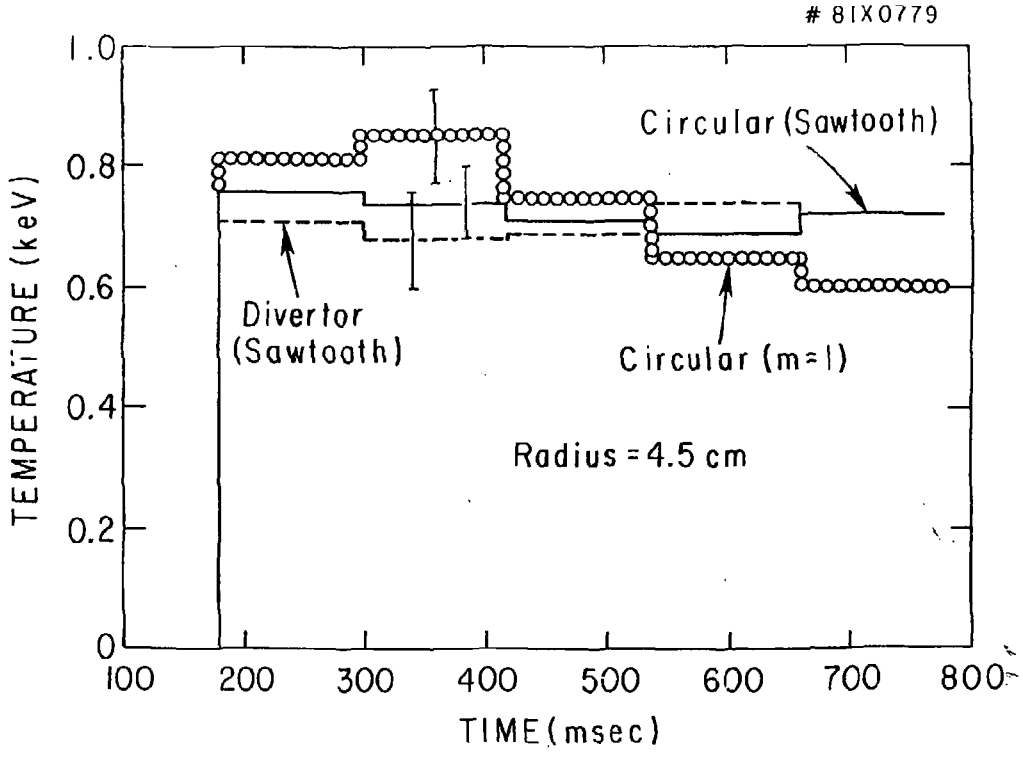
81X0779
1.0
0.8
0.6
0.4
0.2
0
TEMPERATURE (keV)
100
200
300
400
500
600
700
800
TIME (msec)
Circular (Sawtooth)
Divertor
(Sawtooth)
Circular (m=1)
Radius = 4.5 cm

Fig. 14

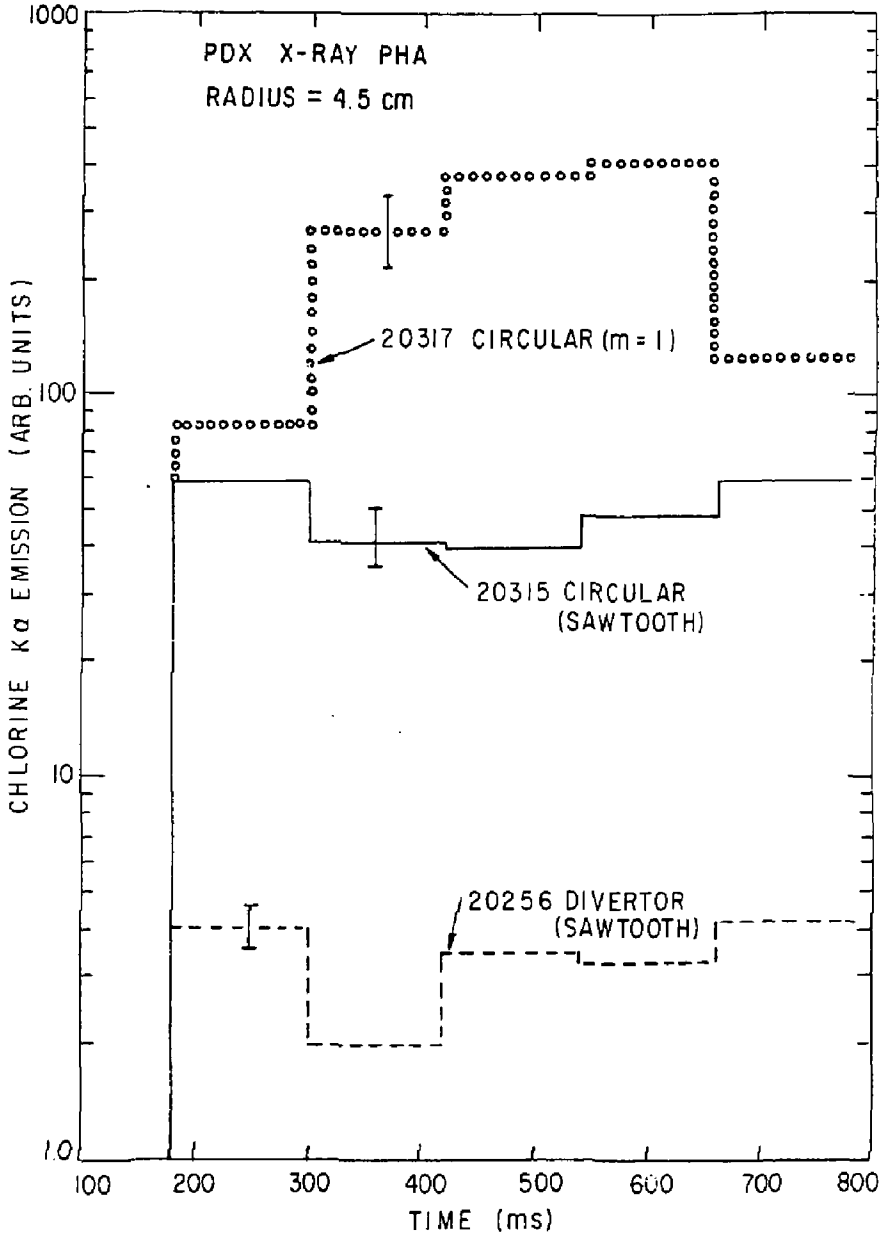
PDX X-RAY PHA
RADIUS = 4.5 cm
20317 CIRCULAR (m = 1)
20315 CIRCULAR
(SAWTOOTH)
20256 DIVERTOR
(SAWTOOTH)
CHLORINE Kα EMISSION (ARB. UNITS)
1000
100
10
1.0
100
200
300
400
500
600
700
800
TIME (ms)

Fig. 15

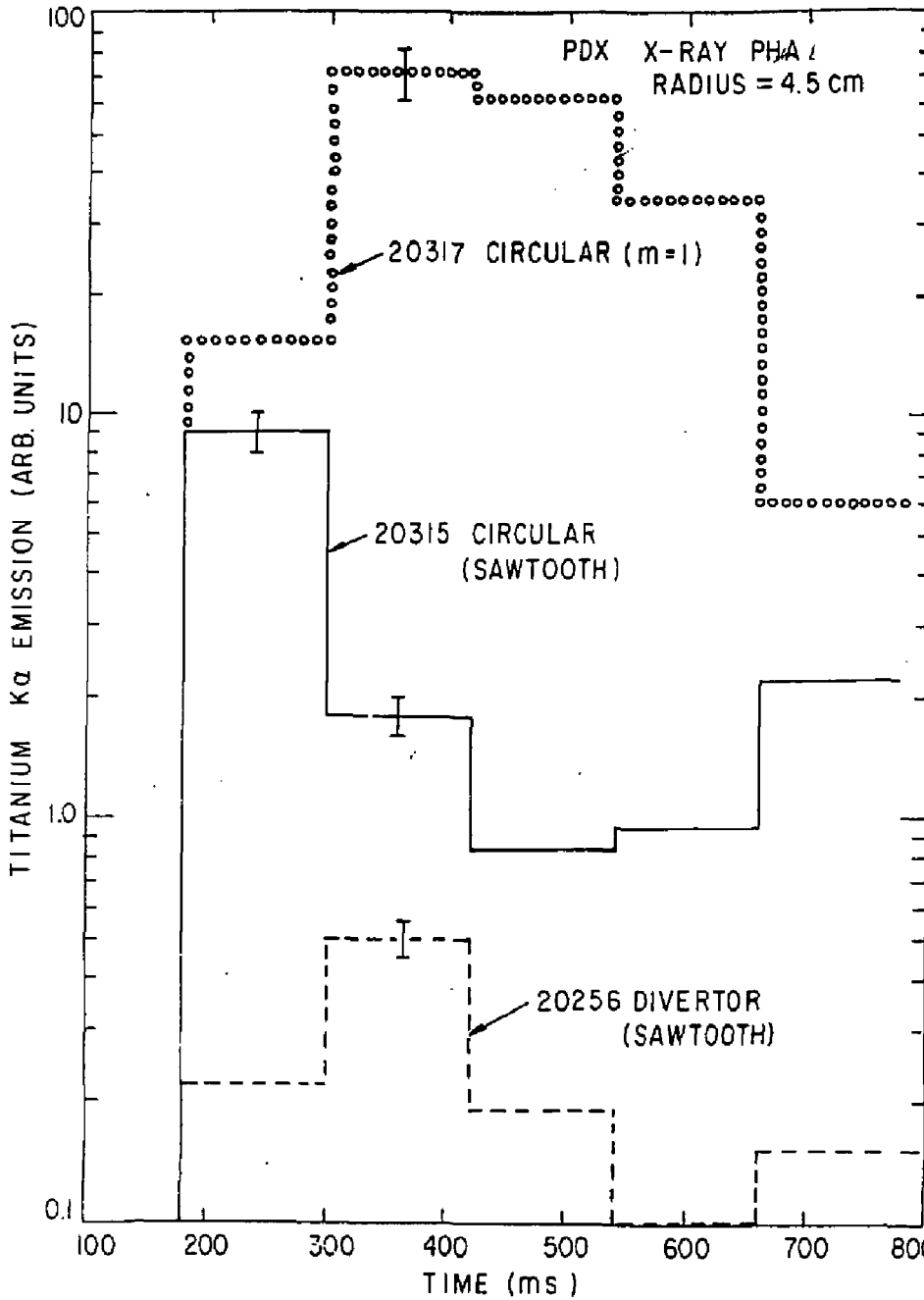
PDX X-RAY PHA
RADIUS = 4.5 cm
20317 CIRCULAR (m=1)
20315 CIRCULAR
(SAWTOOTH)
20256 DIVERTOR
(SAWTOOTH)
TITANIUM Kα EMISSION (ARB. UNITS)
TIME (ms)
100
10
1.0
0.1
100
200
300
400
500
600
700
800

Fig. 16

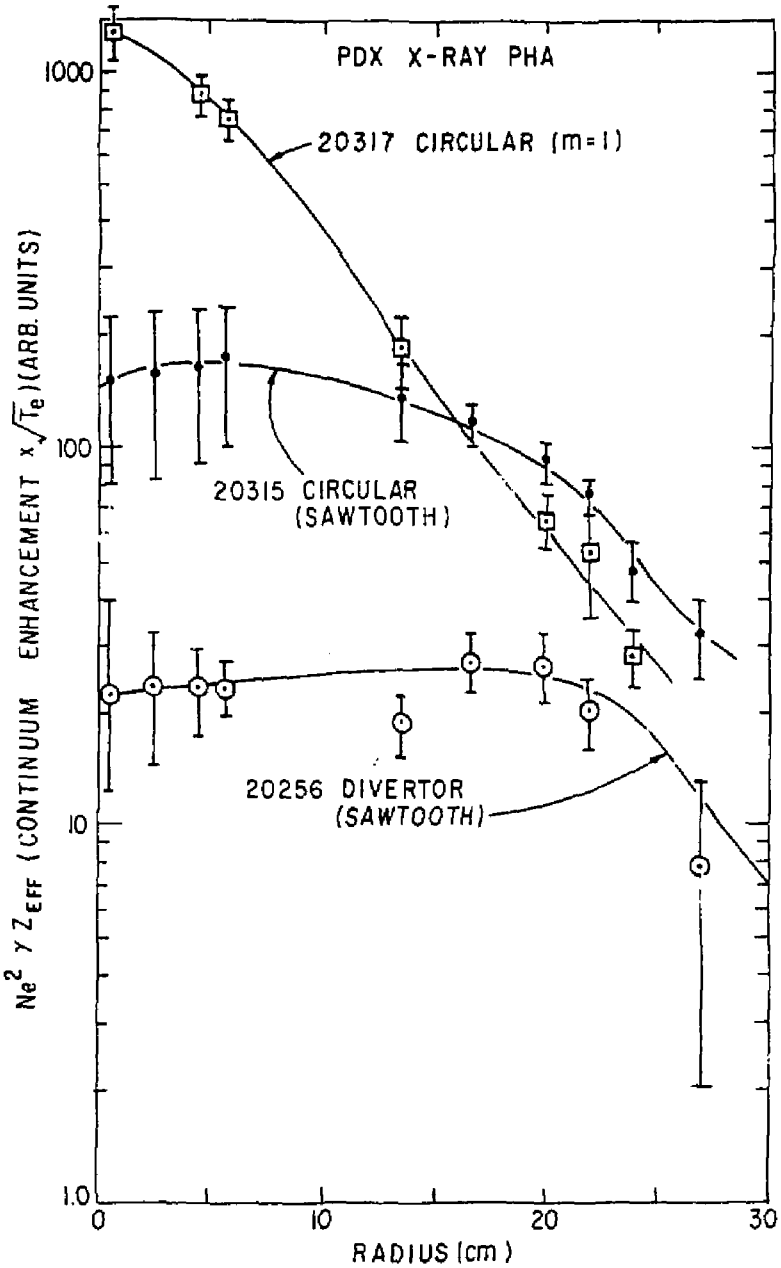
PDX X-RAY PHA
20317 CIRCULAR (m=1)
20315 CIRCULAR
(SAWTOOTH)
20256 DIVERTOR
(SAWTOOTH)
1000
100
10
1.0
0
10
20
30
RADIUS (cm)
Ne² γ Z_EFF (CONTINUUM ENHANCEMENT x √Te) (ARB. UNITS)

Fig. 17

A TIME SERIES OF PHOTONS OCCURRING AT AVERAGE RATE 'a'

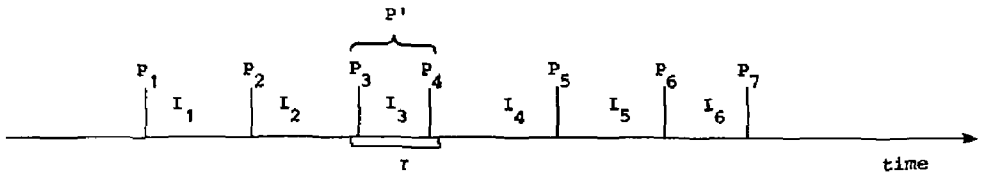

WITHOUT PILEUP

7 Photons: P_1, P_2, P_3, P_4, P_5, P_6, P_7

6 Intervals: I_1, I_2, I_3, I_4, I_5, I_6

WITH PILEUP

6 Photons: P_1, P_2, P_3, + $P_4 \simeq P'$, P_5, P_6, P_7

5 Intervals: I_1, I_2, I_4, I_5, I_6

In General:

For large number of N intervals, I_1, I_2, ..., I_N

$I_j \leq \tau$ n times where $n = N(1-e^{-a\tau})$ and $a = N/t$.

The measured rate is $a_M \cong a - a^2\tau$.

Fig. A.1

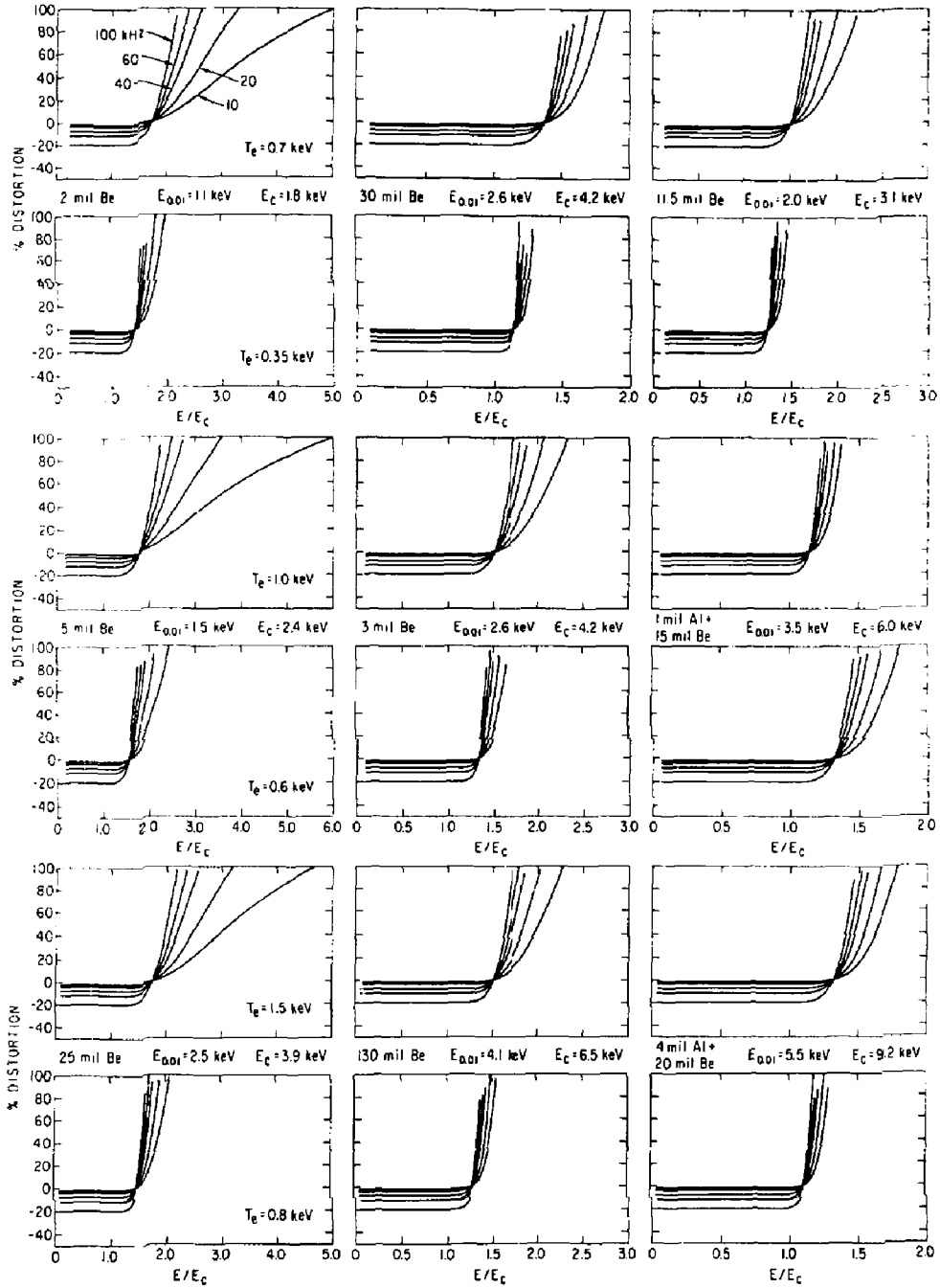
% DISTORTION
100 kHz
60
40
20
10
T_e = 0.7 keV
2 mil Be $E_{0.01}$ = 1.1 keV E_c = 1.8 keV
30 mil Be $E_{0.01}$ = 2.6 keV E_c = 4.2 keV
11.5 mil Be $E_{0.01}$ = 2.0 keV E_c = 3.1 keV
T_e = 0.35 keV
T_e = 1.0 keV
5 mil Be $E_{0.01}$ = 1.5 keV E_c = 2.4 keV
3 mil Be $E_{0.01}$ = 2.6 keV E_c = 4.2 keV
1 mil Al + 15 mil Be $E_{0.01}$ = 3.5 keV E_c = 6.0 keV
T_e = 0.6 keV
T_e = 1.5 keV
25 mil Be $E_{0.01}$ = 2.5 keV E_c = 3.9 keV
130 mil Be $E_{0.01}$ = 4.1 keV E_c = 6.5 keV
4 mil Al + 20 mil Be $E_{0.01}$ = 5.5 keV E_c = 9.2 keV
T_e = 0.8 keV
E/E_c

Fig. B.1

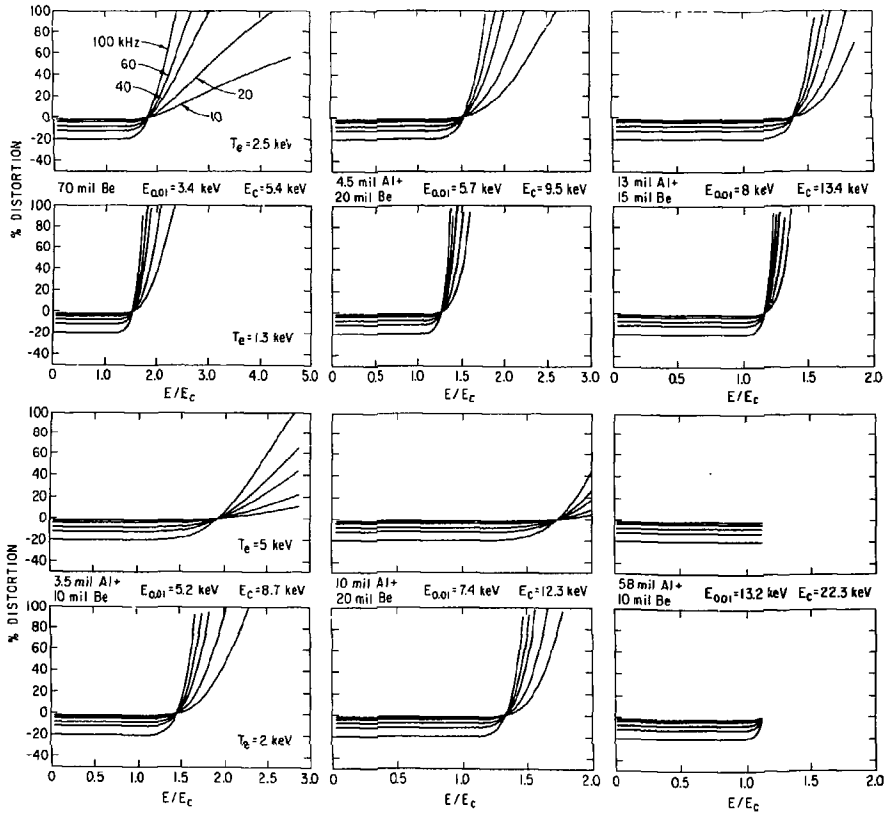
% DISTORTION
100 kHz
60
40
20
10
T_e = 2.5 keV
70 mil Be
$E_{0.01}$ = 3.4 keV
E_c = 5.4 keV
4.5 mil Al+
20 mil Be
$E_{0.01}$ = 5.7 keV
E_c = 9.5 keV
13 mil Al+
15 mil Be
$E_{0.01}$ = 8 keV
E_c = 13.4 keV
T_e = 1.3 keV
E/E_c
3.5 mil Al+
10 mil Be
$E_{0.01}$ = 5.2 keV
E_c = 8.7 keV
10 mil Al+
20 mil Be
$E_{0.01}$ = 7.4 keV
E_c = 12.3 keV
58 mil Al+
10 mil Be
$E_{0.01}$ = 13.2 keV
E_c = 22.3 keV
T_e = 5 keV
T_e = 2 keV

Fig. B.1

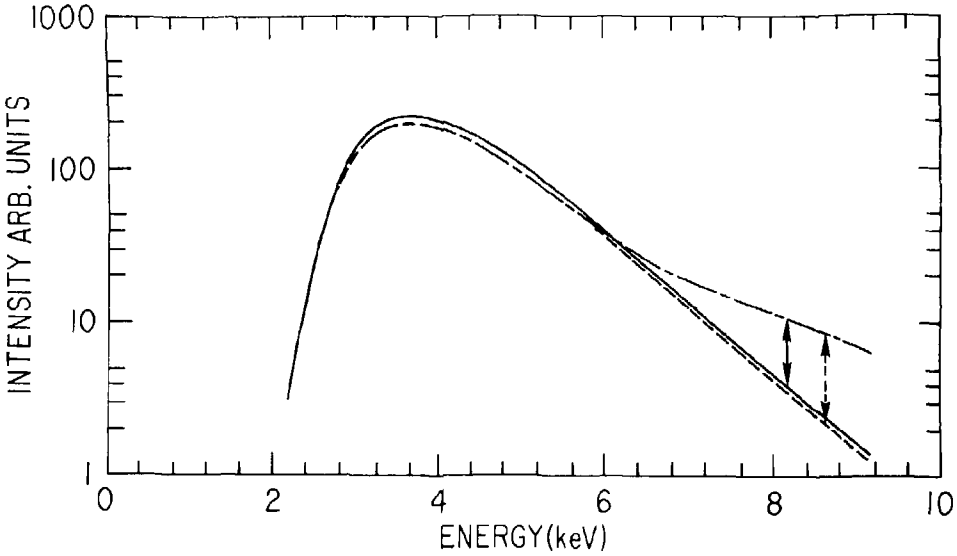

Fig. B.2

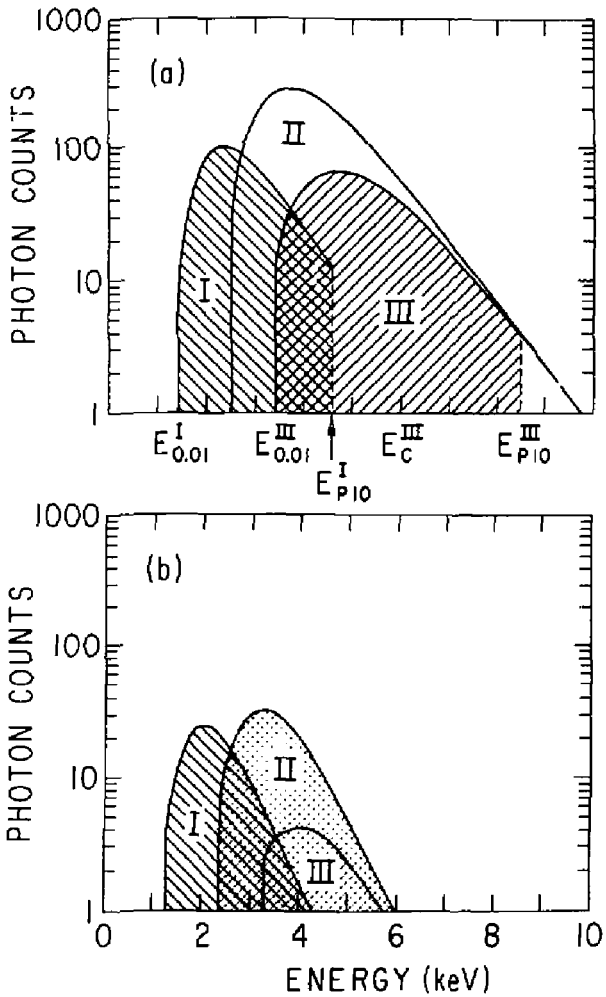

3 DETECTORS

Foil		Relative Aperture Size	Thickness (mils)
I	BE	1	5
II	BE	30	30
III	AL	40	1
	BE		15

Temperature - 1.0 keV
Foil Transmission
I - 1790 Counts
II - 6600 Counts
III - 1740 Counts
} in 60 msec

Temperature - 0.6 keV
Foil Transmission
I - 332 Counts
II - 536 Counts
III - 70 Counts
} in 60 msec

Fig. B.3

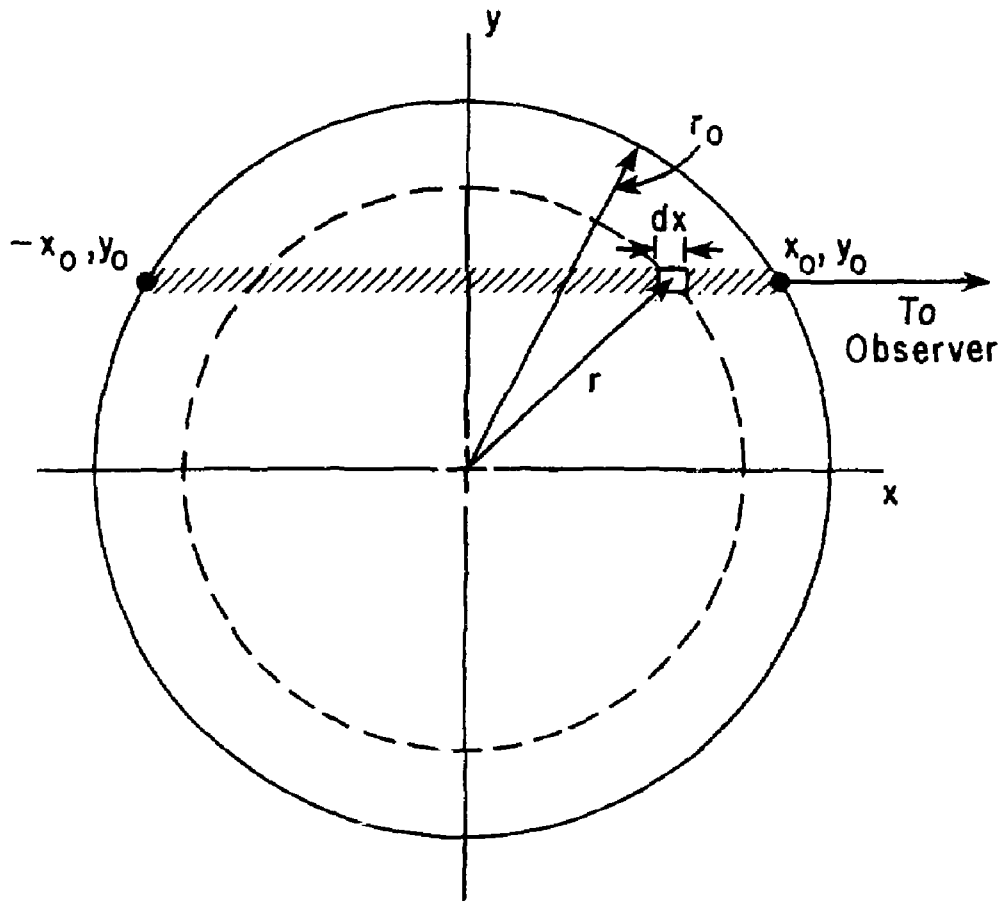

Fig. D.1

EXTERNAL DISTRIBUTION IN ADDITION TO TIC UC-20

ALL CATEGORIES

R. Askew, Auburn University, Alabama
S. T. Wu, Univ. of Alabama
Geophysical Institute, Univ. of Alaska
G.L. Johnston, Sonoma State Univ, California
H. H. Kuehl, Univ. of S. California
Institute for Energy Studies, Stanford University
H. D. Campbell, University of Floride
N. L. Oleson, University of South Florida
W. M. Stacey, Georgia Institute of Technology
Benjamin Ma, Iowa State University
Magne Kristiansen, Texas Tech. University
W. L. Wiese, Nat'l Bureau of Standards, Wash., D.C.
Australian National University, Canberra
C.N. Watson-Munro, Univ. of Sydney, Australia
F. Cap, Inst. for Theo. Physics, Austria
Dr.M. Heindler, Institute for Theoretical Physics Technical University of Graz
Ecole Royale Militaire, Bruxelles, Belgium
D. Palumbo, C. European Comm. B-1049-Brussels
P.H. Sakanaka, Instituto de Fisica, Campinas, Brazil
M.P. Bachynski, MPB Tech., Ste. Anne de Bellevue, Quebec, Canada
C. R. James, University of Alberta, Canada
T.W. Johnston, INRS-Energie, Vareenes, Quebec
H. M. Skarsgard, Univ. of Saskatchewan, Canada
Inst. of Physics, Academia Sinica, Peking, People's Republic of China
Inst. of Plasma Physics, Hefei, Anhwei Province, People's Republic of China
Library, Tsing Hua Univ., Peking, People's Republic of China
Zhengwu Li, Southwestern Inst. of Phys., Leshan, Sichuan Province, People's Republic of China
Librarian, Culham Laboratory, Abingdon, England (2)
A.M. Dupas Library, C.E.N.-G, Grenoble, France
Central Res. Inst. for Physics, Hungary
S. R. Sharma, Univ. of Rajasthan, JAIPUR-4, India
R. Shingal, Meerut College, India
A.K. Sundaram, Phys. Res. Lab., India
Biblioteca, Frascati, Italy
Biblioteca, Milano, Italy
G. Rostagni, Univ. Di Padova, Padova, Italy
Preprint Library, Inst. de Fisica, Pisa, Italy
Library, Plasma Physics Lab., Gokasho, Uji, Japan
S. Mori, Japan Atomic Energy Res. Inst., Tokai-Mura
Research Information Center, Nagoya Univ., Japan
S. Shioda, Tokyo Inst. of Tech., Japan
Inst. of Space & Aero. Sci., Univ. of Tokyo
T. Uchida, Univ. of Tokyo, Japan
H. Yamato, Toshiba R. & D. Center, Japan
M. Yoshikawa, JAERI, Tokai Res. Est., Japan
Dr. Tsuneo Nakakita, Toshiba Corporation, Kawasaki-Ku Kawasaki, 210 Japan
N. Yajima, Kyushu Univ., Japan
R. England, Univ. Nacional Auto-noma de Mexico
B. S. Liley, Univ. of Waikato, New Zealand
S. A. Moss, Saab Univas Norge, Norway
J.A.C. Cabral, Univ. de Lisboa, Portugal
O. Petrus, AL.I. CUZA Univ., Romania
J. de Villiers, Atomic Energy Bd., South Africa
A. Maurech, Comisaria De La Energy y Recoursos Minerales, Spain
Library, Royal Institute of Technology, Sweden
Cen. de Res. En Phys.Des Plasmas, Switzerland
Librarian, Fom-Instituut Voor Plasma-Fysica, The Netherlands
Bibliothek, Stuttgart, West Germany
R.D. Buhler, Univ. of Stuttgart, West Germany
Max-Planck-Inst. fur Plasmaphysik, W. Germany
Nucl. Res. Estab., Julich, West Germany
K. Schindler, Inst. Fur Theo. Physik, W. Germany

EXPERIMENTAL
THEORETICAL

M. H. Brennan, Flinders Univ. Australia
H. Barnard, Univ. of British Columbia, Canada
S. Screenivasan, Univ. of Calgary, Canada
J. Radet, C.E.N.-B.P., Fontenay-aux-Roses, France
Prof. Schatzman, Observatoire de Nice, France
S. C. Sharma, Univ. of Cape Coast, Ghana
R. N. Aiyer, Laser Section, India
B. Buti, Physical Res. Lab., India
L. K. Chavda, S. Gujarat Univ., India
I.M. Las Das, Banaras Hindu Univ., India
S. Cuperman, Tel Aviv Univ., Israel
E. Greenspan, Nuc. Res. Center, Israel
P. Rosenau, Israel Inst. of Tech., Israel
Int'l. Center for Theo. Physics, Trieste, Italy
I. Kawakami, Nihon University, Japan
T. Nakayama, Ritsumeikan Univ., Japan
S. Nagao, Tohoku Univ., Japan
J.I. Sakai, Toyama Univ., Japan
S. Tjotta, Univ. I Bergen, Norway
M.A. Hellberg, Univ. of Natal, South Africa
H. Wilhelmson, Chalmers Univ. of Tech., Sweden
Astro. Inst., Sonnenborgh Obs., The Netherlands
T. J. Boyd, Univ. College of North Wales
K. Hubner, Univ. Heidelberg, W.Germany
H. J. Kaeppeler, Univ. of Stuttgart, West Germany
K. H. Spatschek, Univ. Essen, West Germany

EXPERIMENTAL
ENGINEERING

B. Grek, Univ. du Quebec, Canada
P. Lukac, Komenskeho Univ., Czechoslovakia
G. Horikoshi, Nat'l Lab for High Energy Physics, Tsukuba-Gun, Japan

EXPERIMENTAL

F. J. Paoloni, Univ. of Wollongong, Australia
J. Kistemaker, Fom Inst. for Atomic & Molec. Physics, The Netherlands

THEORETICAL

F. Verheest, Inst. Vor Theo. Mech., Belgium
J. Teichmann, Univ. of Montreal, Canada
T. Kahan, Univ. Paris VII, France
R. K. Chhajlani, India
S. K. Trehan, Panjab Univ., India
T. Namikawa, Osaka City Univ., Japan
H. Narumi, Univ. of Hiroshima, Japan
Korea Atomic Energy Res. Inst., Korea
E. T. Karlson, Uppsala Univ., Sweden
L. Stenflo, Univ. of UMEA, Sweden
J. R. Saraf, New Univ., United Kingdom